

1 **Energetic Particle injection, acceleration, and loss during the**  
2 **geomagnetic disturbances which upset Galaxy 15**

3

4 Mark A. Clilverd

5 British Antarctic Survey, Cambridge, United Kingdom.

6 Craig J. Rodger

7 Department of Physics, University of Otago, Dunedin, New Zealand.

8 Donald Danskin

9 Geomagnetic Laboratory, Natural Resources Canada, Ottawa, Canada.

10 Maria E. Usanova

11 Department of Physics, University of Alberta, Edmonton, Canada.

12 Tero Raita, Thomas Ulich

13 Sodankylä Geophysical Observatory, University of Oulu, Sodankylä, Finland.

14 Emma L. Spanswick

15 University of Calgary, Calgary, Canada.

16

17

18 **Abstract.** On 05 April 2010 a series of energetic electron injections, acceleration, and  
19 loss events appeared to induce an operational anomaly in the Galaxy 15 geosynchronous  
20 communications satellite [Allen, 2010]. We describe the energetic electron precipitation  
21 (EEP) conditions leading to the anomaly. A few hours prior to the anomaly electron  
22 acceleration at  $>0.6$  MeV, and loss at  $> 30$  keV, were observed simultaneously. The  
23 acceleration took place in the region of the Galaxy 15 satellite on the nightside, and the  
24 precipitation of electrons primarily on the dayside. The precipitation was confined to  $L$ -

25 shells outside of the plasmapause, and appeared to be driven by chorus waves via a weak  
26 diffusion process. An hour prior to the anomaly, a solar wind shock event generated a  
27 few minutes of 30-150 keV electron precipitation but only on the dayside, over a large  $L$ -  
28 shell range ( $4.8 < L < 13$ ). The timing of the precipitation burst was consistent with EMIC  
29 waves seen on the dayside, but the high geomagnetic latitude of the precipitation suggests  
30 that EMIC wave growth associated with high cold density regions in the plasmasphere is  
31 unlikely to have played a role. A substorm injection event shortly after the shock appears  
32 to have ultimately triggered the upset on Galaxy 15. However, the peak  $>30$  keV electron  
33 precipitation fluxes of  $1.35 \times 10^7$  el.  $\text{cm}^{-2}\text{s}^{-1}\text{sr}^{-1}$  were roughly the same level as other large  
34 substorm events previously analyzed, indicating either a sensitivity to the energetic  
35 electron environment prior to the event or that the satellite was in a vulnerable situation.

36

## 37 **1. Introduction**

38 On the 5<sup>th</sup> April 2010 a CME-driven solar wind shock compressed the Earth's magnetosphere,  
39 and induced an operational anomaly in the Galaxy 15 geosynchronous communications satellite  
40 [Allen, 2010] which was close to MLT midnight at the time. The shock arrived at the Earth at  
41 08:25 UT. Magnetospheric conditions following the compression have been comprehensively  
42 described by Connors et al. [2011]. Large dipolarisations were observed by THEMIS spacecraft  
43 in the midnight sector near  $X=-11$ ,  $Y=-2 R_e$ , and a large flux transfer into the inner  
44 magnetosphere took place. The extreme geophysical conditions produced a substorm that began  
45 at 09:03 UT which appeared to induce the anomalies, and subsequent loss of control, in the  
46 Galaxy 15 geostationary communications satellite at 09:48 UT [Connors et al., 2011]. We will  
47 therefore refer to this series of events as the Galaxy 15 period, made up of three event periods,  
48 the last of which is the Galaxy 15 substorm.

49 During the Galaxy 15 substorm period several different processes could have produced  
50 energetic electron precipitation (EEP) into the atmosphere. One of these processes was the  
51 substorm itself, and although EEP is a well known consequence of substorm occurrence in that  
52 clear signatures of substorms are often observed with riometer instruments [Berkey et al., 1974;  
53 Spanswick et al., 2009; Clilverd et al., 2012], this particular substorm is worthy of investigation  
54 as an example of an extreme event. Another process that has previously been reported to  
55 generate electron precipitation into the atmosphere is the solar wind shock itself [e.g., Clilverd et  
56 al., 2007]. Studies by Zhou and Tsurutani [1999], and Tsurutani et al. [2001] have suggested that  
57 the adiabatic compression can lead to a loss cone instability, wave growth and enhanced pitch  
58 angle scattering leading to EEP. The mechanism through which EEP could occur during the  
59 shock is unclear, but could include wave-particle interactions from EMIC waves [Fuselier et al.,  
60 2004], chorus waves [Longden et al., 2008], or due to a compression-driven lowering of the  
61 mirror points of trapped particles to altitudes below  $\sim 100$  km [Spann et al., 1998]. EEP from

62 EMIC waves has been reported by Rodger et al. [2008a] and Miyoshi et al. [2008] typically  
63 occurring on the evening side, close to the geomagnetic latitude of the plasmapause. Low-energy  
64 electron precipitation ( $\sim 200$  eV) by chorus waves has been associated with auroral forms [Ni et  
65 al., 2011], and through theoretical studies of wave-particle interactions [Horne, 2002; Horne et  
66 al., 2005]. The association of chorus wave with EEP is less certain.

67 Understanding the occurrence, and driving mechanisms, of EEP into the atmosphere is an  
68 important requirement, both in determining the role of electron losses from the magnetosphere  
69 [Reeves et al., 2003; Clilverd et al., 2006; Hendry et al., 2012], and the subsequent impact of  
70 EEP on the atmosphere [e.g., Seppala et al., 2007; 2009]. Further, the competing roles of  
71 electron acceleration and loss result in the complex response of the outer radiation belt to  
72 geomagnetic storms [Reeves et al., 2003] and the consequent difficulty in providing accurate  
73 space weather predictions for the satellite industry [Fok et al., 2008]. Electron losses into the  
74 atmosphere could reduce any hazard to satellites from electron acceleration processes or  
75 substorm injections, and identifying the characteristics of EEP could provide some information  
76 about loss mechanisms taking place. Furthermore, electron precipitation can be a signature of the  
77 acceleration processes taking place in the radiation belt, as the wave-particle interactions which  
78 accelerate some electrons also precipitate a large fraction [e.g., Hendry et al., 2012]. Accurate  
79 measurements of EEP are difficult to make from spacecraft because the detectors either measure  
80 only a fraction of the bounce loss cone, or include some of the drift loss cone, or include some of  
81 the trapped component of the radiation belts [Rodger et al., 2010a]. Ground-based measurements  
82 of EEP characteristics rely on monitoring the changes in D-region ionization caused by the  
83 precipitation [Rodger et al., 2012]. These techniques effectively use the ionosphere as a large  
84 particle detector [Clilverd et al., 2009], but only by using multi-instrument ground-based  
85 observations of the ionization produced by EEP is it possible to accurately characterize the EEP  
86 events.

87 The enhanced ionization caused by EEP can produce odd nitrogen (NO<sub>x</sub>) and odd hydrogen  
88 (HO<sub>x</sub>) species in the upper and middle atmosphere [Brasseur and Solomon, 2005]. HO<sub>x</sub> is short  
89 lived but responsible for the catalytic ozone loss at mesospheric altitudes [Verronen et al., 2011],  
90 while NO<sub>x</sub> is much longer-lasting in the absence of sunlight, and can be transported to lower  
91 altitudes where it can catalytically destroy ozone in the stratosphere, particularly at the poles  
92 [Randall et al., 2005; Seppala et al., 2009]. Radiation belt processes can generate EEP for long  
93 periods, i.e., up to ~10 days [Rodger et al., 2010b; Clilverd et al., 2010], and have been shown to  
94 generate EEP in large enough amounts to cause observable chemical changes in the upper  
95 atmosphere [Verronen et al., 2011; Andersson et al., 2012]. However, such extended periods of  
96 precipitation can be made up of several different class of event, with different characteristic  
97 energy spectra, MLT distributions, temporal variations, and fluxes. As such, it is important that  
98 the different driving mechanisms of EEP are understood in detail.

99 Connors et al. [2011] noted that significant particle injections were observed during the  
100 Galaxy 15 substorm, but did not undertake any detailed descriptions. In this study we describe  
101 the energetic electron precipitation which occurred throughout the Galaxy 15 period using  
102 ground-based instrumentation, and relate it to electron detector measurements made at the same  
103 time by spacecraft, such as GOES and POES. We discuss in detail the energetic electron  
104 precipitation characteristics observed before the arrival of the solar wind shock event, during the  
105 shock itself, and as a result of the large substorm injection which occurred shortly after the  
106 shock. We compare the observations made over a range of magnetic local times, and discuss the  
107 driving mechanisms that might account for the energetic electron precipitation that occurred.

## 109 2. Geomagnetic conditions

110 The geomagnetic conditions during the Galaxy 15 period are summarized in Figure 1. The plot  
111 shows the solar wind parameters and geomagnetic indices from 00-12 UT on 05 April 2010.  
112 From top to bottom the panels show the variation of the solar wind speed and density, IMF Bz,  
113 and the AE and AO geomagnetic indices. The Bz panel indicates that predominantly negative Bz  
114 existed during most of the study period, with significant geomagnetic disturbance levels  
115 occurring after ~08 UT, including periods of large positive Bz. The ~09 UT substorm event was  
116 initiated by a sudden solar wind shock at ~08:25 UT shown by the sudden increase in solar wind  
117 speed and density, and highlighted by the dashed vertical line. The solar wind speed increased  
118 from an already high level of  $\sim 500 \text{ km s}^{-1}$  to  $\sim 750 \text{ km s}^{-1}$  at the time of the shock, with a  
119 simultaneous six-fold increase in solar wind density. These characteristics are consistent with the  
120 arrival of a solar wind stream interface. In all panels the time of the shock arrival at the Earth is  
121 indicated by the dashed vertical line.

122 The geomagnetic indices AE and AO are plotted in the lowest panel of Figure 1. Variations in  
123 both indices show a large disturbance at 09 UT, but also some geomagnetic activity prior to the  
124 shock arrival, starting at ~04:30 UT and lasting until ~ 08 UT. The 04:30 UT disturbance levels  
125 are co-incident with the period of negative Bz seen in the panel above. In summary, the CME-  
126 driven compressional shock that arrived at Earth at 08:25 UT produced severely disturbed  
127 geomagnetic conditions providing additional forcing to a magnetosphere that was already  
128 moderately disturbed, primarily by already high solar wind speeds, and recurring periods of  
129 negative Bz.

130

## 131 3. Experimental setup

132 This study combines ground-based and satellite observations of energetic electron fluxes or  
133 their influence on D-region ionization. On the ground we make use of riometer absorption

134 measurements, broadband 0.5-10 kHz radio wave observations (VELOX), and very low  
135 frequency radio wave observations of man-made transmissions in the range 15-45 kHz  
136 (AARDDVARK). In space we make use of the GOES-11 electron detector, and all six of the  
137 POES satellites then operational, using both their parallel and field-aligned electron telescopes.  
138 Figure 2 shows the MLT distribution of the observations made at 06 UT and 09 UT on 05 April  
139 2010, indicating the sites and satellite locations used in the analysis later in this study. On the  
140 06 UT left-hand panel the Macquarie Island and Abisko riometer stations cover both the  
141 duskside and the dayside. VLF broadband wave data provided by the VELOX instrument comes  
142 from Halley close to MLT dawn. The GOES-11 satellite was in the MLT evening side, and the  
143 Galaxy 15 satellite was nearby [Connors et al., 2011]. On the 09 UT right-hand panel the  
144 Macquarie Island and Dawson riometers are on the evening- and midnight-side respectively,  
145 while Abisko is very close to MLT noon. The GOES-11 satellite was close to MLT midnight,  
146 with the Galaxy 15 satellite nearby. AARDDVARK data from subionospheric propagation paths  
147 indicated by the red lines linking transmitters to receivers (red dots) span the dayside using a  
148 receiver at Sodankylä, and the nightside using receivers at Scott Base and Casey in the Antarctic.  
149 Sodankylä also provides the pulsation magnetometer data used in this study, although it actually  
150 comes from a magnetometer at the same longitude but slightly further south, i.e., Rovaniemi,  
151 Finland. POES data from the multiple satellite configuration is longitudinally averaged in order  
152 to provide 1 hour timing resolution.

153 The riometer data used in this study are provided from Macquarie Island (54.5°S, 158.9°E,  
154  $L=5.4$ ), Dawson, Canada (64.05°N, 220.89 °E,  $L=6.0$ ), and Abisko, Sweden (68.4°N, 18.9°E,  
155  $L=5.9$ ). Riometers [Little and Leinbach, 1959] observe the integrated absorption of cosmic radio  
156 noise through the ionosphere, with increased absorption due to additional ionization, for example  
157 due to both proton and electron precipitation. Typically the riometer absorption is provided by a  
158 widebeam, 30 MHz, vertically pointing antenna. The dominant altitude of the absorption is

159 typically in the range 70-100 km, i.e., biased towards relatively soft particle energies (~30 keV  
160 electrons).

161 The VELOX instrument (VLF/ELF Logger Experiment) is an experiment to record  
162 continuously, on a long term basis, the VLF radio noise characteristics in 10 frequency bands  
163 between 0.5-9.3 kHz [Smith, 1995]. Located at Halley, Antarctica (75.5°S, 26.3°W,  $L=4.5$ ) the  
164 VELOX instrument is situated in an environment that is practically free from any man-made  
165 interference, and hence is ideally situated to monitor inner magnetospheric VLF wave activity  
166 close to the plasmapause, such as chorus and hiss in the 1-3 kHz range [Rodger and Clilverd,  
167 2008b]. Smith et al. [2010] showed that chorus and hiss waves in the 1-3 kHz range were  
168 enhanced at Halley as a result of geomagnetically disturbed conditions ( $K_p > 2$ ). The increase in  
169 amplitude with geomagnetic activity was typically 2-6 dB, and was usually observed over the  
170 period 05-15 UT (03 – 13 MLT) at all times of the year. Thus we would expect the Halley  
171 VELOX instrument to be in an ideal location to provide observations of VLF wave activity  
172 during the period under study in this analysis.

173 AARDDVARK, the Antarctic-Arctic Radiation-belt Dynamic Deposition VLF Atmospheric  
174 Research Konsortia [Clilverd et al., 2009] is a network of VLF receivers operating in the  
175 frequency range 10-50 kHz. Each receiver is capable of receiving narrow-band transmissions  
176 from a number of powerful man-made communication transmitters, which can occasionally be as  
177 much as 15,000 km away. The AARDDVARK network uses narrow band subionospheric  
178 VLF/LF data to observe changes in the D-region ionization levels. This study makes use of the  
179 transmissions on the dayside from NRK (Iceland, 37.5 kHz, 64.2°N, 21.9°W,  $L= 5.57$ ) and GVT  
180 (England, 22.1 kHz, 54.7°N, 2.9°W,  $L=2.65$ ) received at Sodankylä, Finland (67.4°N, 26.7°E,  
181  $L=5.34$ ). The transmitter-receiver paths involved are ~1000 km long. On the nightside signals  
182 from NPM (Hawaii, 21.4 kHz, 21.4°N, 158.1°W,  $L=1.17$ ) and NDK (North Dakota, 25.2 kHz,

183 46.4°N, 98.3°W,  $L=3.24$ ) are examined that have been received at Casey, Antarctica (66.3°S,  
184 110.5°E,  $L>999$ ) and Scott Base, Antarctica (77.8°S, 166.8°E,  $L>32$ ). The transmitter-receiver  
185 paths involved are  $\sim 7,600$  km and  $\sim 9,400$  km respectively. The effects of changing propagation  
186 conditions in the mesosphere, often due to energetic particle precipitation, typically  $>50$  keV  
187 during the night and  $>200$  keV during the day, can be seen as either an increase or decrease in  
188 signal amplitude, and usually an increase in phase, depending on the modal mixture of each  
189 signal observed [Barr et al., 2000; Rodger et al., 2012]. Hence we can use the AARDDVARK  
190 data to indicate the presence of large scale energetic particle precipitation regions.

191 A latitudinal chain of pulsation magnetometers is located in Finland, and operated by the  
192 Sodankylä Geophysical Observatory. The magnetometers range from  $L=3.4-6.1$ , and operate  
193 with a time resolution of 0.025 s. In this study we present magnetometer wave power over the  
194 frequency range 0.25-1.5 Hz from the Rovaniemi site, located at 66.8°N, 25.9°E, and at  $L=5.1$ .  
195 Waves in this frequency range are known as Pc 1-2 pulsations and are generated by the  
196 electromagnetic ion cyclotron (EMIC) instability near the magnetic equator. Pc 1-2 waves  
197 propagate along the field line, and can also be observed on the ground [Erlandson et al., 1996].  
198 Solar wind compressions of the magnetosphere can generate Pc 1 pulsations, as the  
199 compressions increase the ion anisotropy which, in turn, increases the EMIC wave growth rate  
200 [Kangas et al., 1986].

201 Geostationary ( $L=6.6$ ) electron flux data are provided by GOES-11  $>600$  keV and  $>2$  MeV  
202 detectors [Onsager et al., 1996]. At the time of this study GOES-11 was the primary SWPC  
203 satellite for the proton, electron, and magnetometer instruments, and was located at 135°W. The  
204 magnetic local time at 09:00 UT on 05 April 2010 (as shown in Figure 2) was 23:52 MLT, and  
205 thus the satellite was well positioned to observe the effects of substorm-injected energetic  
206 electrons. The GOES-11 D3 dome detector provides both the  $>600$  keV and  $>2$  MeV electron

207 fluxes, primarily responding to trapped outer-radiation belt particles. The relative variations of  
208 the electron fluxes observed at each energy channel are useful for scientific studies. We use the 5  
209 minute averaged GOES data which has been corrected for proton contamination, but also note  
210 that no solar proton event occurred during the study period, so proton contamination is likely to  
211 be minimal.

212 We also make use of particle measurements by the Space Environment Monitor-2 (SEM-2)  
213 instrument package onboard the POES spacecraft which are in Sun-synchronous orbits at ~800-  
214 850 km altitudes [Evans and Greer, 2004]. SEM-2 includes the Medium Energy Proton and  
215 Electron Detector (MEPED), in addition to the Total Energy Detector (TED). Together these  
216 instruments monitor electron fluxes from 50 eV up to 2700 keV. We make use of SEM-2  
217 observations from up to 6 POES spacecraft. The SEM-2 detectors include integral electron  
218 telescopes with energies of >30 keV, >100 keV, and >300 keV, pointed in two directions.

219 All POES data is available from <http://poes.ngdc.noaa.gov/data/> with the full-resolution data  
220 having 2-s time resolution. Analysis by *Rodger et al.* [2010a] indicated that the levels of  
221 contamination by comparatively low energy protons can be significant in the MEPED  
222 observations. As much as ~42% of the 0° telescope >30 keV electron observations were typically  
223 found to be contaminated, although the situation was less marked for the 90° telescope (3.5%).  
224 However, NOAA has developed new techniques to remove the proton contamination from the  
225 POES SEM-2 electron observations, as described in Appendix A of *Lam et al.* [2010]. This  
226 algorithm is available for download through the Virtual Radiation Belt Observatory (ViRBO;  
227 <http://virbo.org>), and has been applied to the SEM-2 observations examined in our study. The 0°-  
228 pointing detectors are mounted on the three-axis stabilized POES spacecraft so that the centre of  
229 each detector field of view is outward along the local zenith, parallel to the Earth-centre-to-  
230 satellite radial vector. Another set of detectors, termed the 90°-detectors are mounted  
231 approximately perpendicular to the 0° detector. In addition, there is also a set of omnidirectional

232 measurements made from a dome detector which is mounted parallel to the  $0^\circ$  detectors. The  
233 detectors pointing in the  $0^\circ$  and  $90^\circ$  directions are  $\pm 15^\circ$  wide, while the omnidirectional dome  
234 detectors (termed "omni") are  $\pm 60^\circ$  wide. For the  $3 < L < 10$  range we consider in this study the  
235  $90^\circ$ -detector appears to primarily respond to trapped electrons, and hence we will refer to it as the  
236 "trapped detector", while the  $0^\circ$ -detector is responds to the electrons in the bounce loss cone, and  
237 is thus referred to as the "blc detector" [see the modeling in the Appendix of Rodger et al.,  
238 2010c].

239

### 240 **3. Results**

241 The response of outer radiation belt energetic electron fluxes observed by satellites, and excess  
242 ionospheric ionization associated with electron precipitation into the atmosphere, from 00 –  
243 12 UT on 05 April 2010 is shown in Figure 3. The figure shows panels for the GOES-11  
244  $>0.6$  MeV trapped electron flux at  $L=6.6$ , the POES  $>100$  keV trapped and blc electron flux at  
245  $3 < L < 10$ , and the Abisko riometer absorption at  $L=5.9$ . The time of the solar wind shock hitting  
246 the magnetosphere is identified by a vertical dashed line in all panels. GOES data represents  
247 nightside MLT conditions, POES data is zonally averaged in order to get 1 hour time resolution,  
248 and the Abisko riometer data represents dayside MLT conditions.

249 Three distinct features are apparent in Figure 3. The first is an increase in trapped fluxes at  
250  $>600$  keV and  $>100$  keV at  $\sim 05$  UT, as well as an increase in riometer absorption at the same  
251 time. This follows a small decrease in flux at 05 UT which maybe a result of a weak stretch and  
252 dipolarisation of the magnetic field on the night-side. The POES  $>100$  keV blc electron flux also  
253 shows the same flux-increase feature, and generally tracks the trapped flux variation throughout  
254 the study period, but with flux levels about a factor of 100 lower before the event and a factor of  
255 5 lower during the event. A second feature is a small increase in riometer absorption at the time  
256 of the solar wind shock arrival, i.e., 08:25 UT. This feature is not clearly seen in the satellite

257 data. The third feature is a substantial increase in electron flux observed by satellite, and  
258 increased riometer absorption, at ~09 UT. This is coincident with the timing of the Galaxy 15  
259 substorm.

260 Whereas Figure 3 shows the energetic particle conditions during the period under study,  
261 Figure 4 shows some of the wave activity during the same period. The upper panel shows the  
262 0.5-10 kHz VLF wave intensity recorded at Halley, Antarctica ( $L=4.5$ ), from 00-12 UT on 05  
263 April 2010. Increases in VLF wave intensity in the 1-3 kHz range are observed from 05-08 UT,  
264 at ~08:30 UT, and in the 4-6 kHz range at ~09 UT. These periods coincide with the particle  
265 features indentified in Figure 3. Enhancements in VLF wave activity have been associated with  
266 wave-particle interactions, driving energetic electron acceleration, and loss [Horne et al., 2005].  
267 In the lower panel the Pc 1-2 wave power from Rovaniemi, Finland ( $L=5.1$ ), is shown.  
268 Impulsive, non-structured, noise can be seen at 00 UT, and ~06 UT, with EMIC-like wave  
269 structures occurring at about 0.5 Hz from ~08:30UT. In the following subsections we discuss  
270 each of these features in turn, describing their principle characteristics and potential driving  
271 mechanisms.

272

### 273 **3.1 Wave-induced acceleration and precipitation (03-08 UT)**

274 Prior to the arrival of the solar wind shock at 08:25 UT there was a period of weak  
275 geomagnetic disturbance, as exhibited by AE, which began at 04:30 UT and remained elevated  
276 until ~07 UT. This geomagnetic disturbance appears to be driven by negative IMF  $B_z$  conditions,  
277 with extreme values of ~-5 nT. An apparent consequence of the geomagnetic disturbance is a  
278 period of enhanced trapped fluxes observed by the GOES detectors on the nightside. Figure 5  
279 shows the period from 04:00-08:24 UT, with the upper two panels containing GOES >600 keV  
280 and >2 MeV fluxes respectively. The two riometer panels show nightside Macquarie Island  
281 absorption, and dayside Abisko absorption variations respectively, while the penultimate panel

282 shows the dawnside VLF 2.0 kHz wave intensity at Halley, Antarctica. Typically a factor of 4  
283 increase in trapped flux is observed at >600 keV and >2 MeV, with a slow recovery lasting about  
284 three hours in the GOES data. The VLF waves show a 15 dB increase in intensity at the start of  
285 the event, before declining to pre-event levels by ~08 UT. The two riometer panels showing  
286 nightside Macquarie Island absorption and dayside Abisko absorption variations are set to the  
287 same absorption scale. The nightside riometer observes no enhancement in absorption associated  
288 with EEP during the period when dayside absorption is increased.

289

### 290 **3.2 Compression-induced precipitation (08:25 UT)**

291 At 08:25 UT on 05 April 2010 a solar wind shock arrived at the Earth's magnetosphere, and  
292 initiated a period of geomagnetic disturbance. In Figure 3 the summary plot of this study period  
293 showed that there was an almost immediate response to the arrival of the shock, as was seen by  
294 the ~1 dB enhancement in dayside riometer absorption. In Figure 6 we zoom in on the period  
295 close to the shock arrival time, plotting GOES >600 keV fluxes, Macquarie Island riometer,  
296 Abisko riometer absorption, Rovaniemi Pc 1-2 wave intensity, and Halley VLF wave intensity  
297 from 08:15 to 08:54 UT. The time of the shock arrival is indicated by the vertical dashed line.  
298 The Abisko riometer panel clearly shows enhanced dayside riometer absorption immediately  
299 following the shock arrival which adds to the declining absorption event associated with the  
300 chorus wave activity reported in section 3.1, and peaks at 08:26 UT. Extended analysis of the  
301 Finnish riometer chain suggests that the riometer signal associated with the shock is observed  
302 over a large latitude range (from Hornsund in Svalbard at  $L=13$ , to Rovaneimi in Finland at  
303  $L=5.1$ , i.e., from the uppermost station to mid-way down the chain, but not at the most  
304 equatorward riometers).

305 On the nightside Figure 6 shows that no clear variation is observed by the GOES >600 keV  
306 electron detectors at the time of the shock (>2 MeV not shown, but no clear variation), while the

307 Macquarie Island riometer is similarly unresponsive at 08:25 UT. The Macquarie riometer  
308 absorption does increase after 08:40 UT, which is coincident with the time of a small substorm  
309 reported by Connors et al. [2011].

310 Some of the dayside response to the shock is apparent in Figure 6 through the enhancement of  
311 VLF wave intensity at 2.0 kHz at Halley ( $L=4.5$ ), and the onset of EMIC wave activity at  
312 Rovaniemi in Finland ( $L=5.1$ ). VLF wave activity increased in the range 1.0 - 2.0 kHz, but was  
313 delayed by 5 minutes relative to the onset time of the shock. The EMIC wave activity is seen to  
314 onset at 08: 25 UT at  $\sim 0.5$  Hz, with a peak of wave power at 08:27 UT, continuing until about  
315 10 UT and gradually increasing in frequency to  $\sim 1$  Hz. This is consistent with the characteristics  
316 of an IPDP (intervals of pulsations of diminishing periods) EMIC wave structure which have  
317 previously been associated with relativistic electron precipitation near the plasmapause [Rodger  
318 et al., 2008a].

319

### 320 **3.3 Substorm-injection and precipitation (08:30-11:00 UT)**

321 The geophysical conditions following the shock event produced a substorm that began at  
322 09:03 UT [Connors et al., 2011]. The substorm appeared to induce the anomalies, and  
323 subsequent loss of control, in the Galaxy 15 satellite, and therefore the energetic electron  
324 precipitation of this particular substorm is worthy of investigation as an example of an extreme  
325 event. Figure 7 shows the POES-observed  $>300$  keV b/c flux as a function of UT and L-shell  
326 (left panel) for the day of 05 April 2010. The substorm can be seen as a sudden increase in flux  
327 just after 09 UT, spread over a large range of L-shells ( $L=4-11$ ). The fluxes increased from  
328 typically  $2 \times 10^2$  el.  $\text{cm}^{-2}\text{s}^{-1}\text{sr}^{-1}$  to  $4 \times 10^5$  el.  $\text{cm}^{-2}\text{s}^{-1}\text{sr}^{-1}$  with peak values at  $L\sim 7$ , and factors of  
329  $10\times$  lower precipitating fluxes  $\pm 2$  L-shells either side of the peak. In the  $>30$  keV detector the  
330 equivalent peak fluxes were  $2 \times 10^7$  el.  $\text{cm}^{-2}\text{s}^{-1}\text{sr}^{-1}$  at  $L=7$ , and  $1 \times 10^7$  el.  $\text{cm}^{-2}\text{s}^{-1}\text{sr}^{-1}$  at  $L=6$ . The  
331 right hand panel of Figure 7 shows the substorm impact on riometers on the nightside

332 (Macquarie Island and Dawson) as well as on the dayside (Abisko). An approximate onset time  
333 of the increase in absorption at Macquarie Island is indicated by the vertical dotted line at  
334 08:55 UT. Nighttime absorption levels due to the substorm peaked at 09:07 UT and 6-8 dB, with  
335 a second smaller peak about 30 minutes later. On the dayside the riometer absorption was  
336 ~11 dB, and also showed a double peaked structure, but overall the absorption event was delayed  
337 by 15 minutes relative to the nightside. The increased absorption on the dayside compared with  
338 the nightside is consistent with the enhanced response of a riometer in daylight [Rodger et al.,  
339 2012], and the delay of the onset of the substorm precipitation from nightside to dayside (12  
340 MLT to near 00 MLT in 15 minutes) is consistent with the drift period of ~300 keV electrons at  
341  $L=6$ . The timing of the second peak 30 minutes after the first in all of the riometers is also  
342 consistent with the drift period of ~300 keV electrons at  $L=6$ , suggesting that the electron  
343 precipitation region drifted around the Earth more than once. The right-hand panel of Figure 7  
344 also shows the variation of GOES-11 >600 keV flux during the event (>2 MeV flux not shown,  
345 but exhibited similar variations). Trapped fluxes increased by a factor of ~20 and GOES  
346 observations indicate that electrons with energies >2 MeV were injected during the substorm.

347 The substorm also produced well defined effects on VLF radio propagation conditions, both  
348 on the nightside and the dayside. Figure 8, upper panel, shows AARDDVARK data received at  
349 Sodankylä using signals from two transmitters on the dayside, Iceland- Sodankylä (NRK-SGO,  
350 37.5 kHz,  $L\sim 5-6$ ), and UK- Sodankylä (GVT-SGO, 22.1 kHz,  $2.5 < L < 5.3$ ). Both phase (dashed  
351 lines) and amplitude (solid line) are shown for each transmitter-receiver path, with the same time  
352 of onset as Figure 7 shown as a vertical dotted line (08:55 UT). The lower panel shows  
353 AARDDVARK data from two transmitters received at Antarctic stations on the nightside,  
354 Hawaii-Casey (NPM-CAS, 21.4 kHz,  $1 < L < 999$ ), and North Dakota-Scott Base (NDK-SB,  
355 25.2 kHz,  $1 < L < 32$ ). Both of the transmitter-receiver paths on the nightside cross the geomagnetic  
356 equator, are very long, and only part of the path is influenced by the substorm precipitation. As a

357 result they are quite complicated to analyze. However, we can see that in all four paths the phase  
358 increases during the substorm, with changes in the order of  $100^\circ$ , and the amplitude shows either  
359 increases or decreases. This behavior is consistent with previous observations of substorm effects  
360 on narrow-band radio wave signals [Clilverd et al., 2012 and references therein]. Only the NRK-  
361 SGO path, which is a quasi-constant  $L$ -shell path near  $L=6$ , shows a double peak pattern in both  
362 phase and amplitude, with the initial peak occurring at  $\sim 09:18$  UT, followed by the second  
363 smaller peak about 30 minutes later. The temporal variation in the NRK-SGO phase and  
364 amplitude is similar to that observed in the riometer data, whereas the other paths with greater  
365 geomagnetic latitude range do not show any obvious response at the time of the second peak,  
366 suggesting that the precipitation associated with the second peak is constrained in latitude, and  
367 centered on  $L\sim 6$ .

368

## 369 **4. Discussion**

### 370 **4.1 Wave-induced acceleration and precipitation (03-08 UT)**

371 Horne et al. [2005] and Xiao et al. [2010 and references therein] suggest that wave-particle  
372 interactions between seed population electrons and chorus waves can provide an acceleration  
373 mechanism that enhances the fluxes of relativistic electrons, particularly those at  $\sim 1$  MeV.  
374 Superluminous waves (Auroral Kilometric Radiation) could also produce the stochastic  
375 acceleration of electrons [Xiao et al., 2007] if those waves are present in the radiation belts under  
376 appropriate conditions. In particular, Xiao et al. [2012] have found that Z-mode waves can yield  
377 rapid acceleration of radiation belt electrons. In Figure 4 and Figure 5 our observations during  
378 the 04-08 UT event suggest that 1-3 kHz chorus waves are present and enhanced, at least on the  
379 dawnside. In the MLT-wave pattern cartoon developed by Summers et al. [1998], and shown as  
380 Figure 7 in that paper, the influence of chorus waves on wave-particle interactions covers the  
381 MLT region from somewhat before midnight, through the dawnside, to near midday. Thus the

382 presence of chorus waves on the dawnside is consistent with the observation of enhanced  
383 electron fluxes in GOES-11 at midnight as a result of wave-induced electron acceleration.

384 In addition to electron acceleration occurring on the nightside and dawnside, Figure 5 also  
385 shows that electron precipitation occurred in this period on the dayside but not on the nightside.  
386 The Abisko riometer showed a maximum of 4 dB of absorption during the wave-induced  
387 acceleration event, peaking just before 06 UT, and slowly declining until ~08 UT. The temporal  
388 variation is very similar to the behavior of the GOES-11 trapped electron fluxes. In contrast, the  
389 duskside Macquarie Island riometer, showed very little variation in absorption during this period,  
390 suggesting that no energetic electron precipitation was occurring in that MLT region. This is also  
391 consistent with the suggestion that chorus waves are capable of inducing electron precipitation,  
392 and that the dusk-nighttime location of Macquarie Island at this time is outside of the longitude  
393 of the anticipated chorus-electron interaction region, presumably because of the lack, or weak  
394 intensity, of any chorus waves that may be present in that region [Summers et al., 1998; Horne,  
395 2002]. Inspection of the Finnish riometer chain data for this event  
396 [<http://www.sgo.fi/Data/Riometer/rioData.php>] suggests that the dayside electron precipitation  
397 did not occur below  $L=4.5$ , i.e., was confined outside of the plasmopause, and this is also  
398 consistent with the Summers chorus interaction region cartoon where the plasmopause defines  
399 the inner boundary of the chorus region. The POES  $>100$  keV b/c electron fluxes shown in  
400 Figure 3 indicate a factor of 40 increase in flux from the time just before the start of the event to  
401 the maximum during the event. The  $>300$  keV b/c fluxes (not shown) increased by a factor of 2-  
402 3 at the same time, although the observed pre-event flux levels were at the detector noise floor,  
403 so it is unclear exactly what factor increase occurred at these higher energies. However, we can  
404 ask a simple question at this stage: are the POES b/c fluxes observed large enough to account for  
405 the 4 dB increase in absorption? Here we can calculate the electron energy spectrum (30 keV-  
406 2.5 MeV) using the different POES energy channels, and as in Clilverd et al. [2008; 2012] we

407 can use a simple ionospheric model to describe the balance of electron number density,  $N_e$ , in the  
408 lower ionosphere, based on that given by Rodger et al. [1998], and further described by Rodger  
409 et al. [2007a, 2012]. By calculating height-integrated differential absorption using the method  
410 described in Rodger et al. [2012], we can estimate the riometer absorption generated by the  
411 observed POES energetic electron precipitation fluxes.

412 Using the POES integral b/c fluxes we calculate that the best fit for the e-folding energy of the  
413 precipitating electron spectrum is 55 keV. The POES b/c flux levels, extrapolated to a spectrum  
414 that ranges from 30 keV - 3 MeV, give an Abisko riometer absorption level of 0.5 dB, assuming  
415 daytime conditions and the underlying ionosphere above Abisko taken from the IRI [Rodger et  
416 al., 2012]. This is considerably smaller than observed, and we estimate that we would need to  
417 increase the  $>30$  keV b/c flux from  $5.7 \times 10^4$  el.  $\text{cm}^{-2}\text{s}^{-1}\text{sr}^{-1}$  observed by POES to  $1.7 \times 10^6$  el.  
418  $\text{cm}^{-2}\text{s}^{-1}\text{sr}^{-1}$  in order to reproduce the Abisko 3.5 dB absorption levels shown in Figure 5. That  
419 equates to a factor of 30 multiplication in POES b/c fluxes in order to reproduce the  
420 observations. This is consistent with the idea that the POES b/c detector is only seeing part of the  
421 b/c at geomagnetic latitudes associated with the outer radiation belt, and that some adjustment  
422 needs to be made to the POES b/c fluxes to take into account the orientation of the telescope to  
423 the b/c, and the distribution of electrons within the b/c [Hendry et al., 2012]. Of course we have  
424 only made a rough calculation using the POES data, and more comprehensive studies are needed  
425 which compensate for the use of zonal and meridional averaged POES data in this study.

426

#### 427 **4.2 Compression-induced precipitation (08:25 UT)**

428 At the time of the solar wind compression of the dayside magnetosphere dayside riometer  
429 absorption was observed almost immediately. There are several competing mechanisms by  
430 which such a rapid response could occur. The high compression of the magnetopause and the  
431 outer magnetosphere during the solar wind shock could drive particle precipitation due to

432 lowering of the mirror points of trapped particles to altitudes below  $\sim 100$  km [Spann et al.,  
433 1998]. Zhou and Tsurutani [1999], and Tsurutani et al. [2001] suggested that the adiabatic  
434 compression could lead to a loss cone instability, wave growth, and enhanced pitch angle  
435 scattering. Zhou et al. [2003], using FAST and DSMP auroral imaging, showed that the  
436 precipitation of 1-10 keV electrons was highly isotropic, filling the loss cone, and was likely  
437 driven by adiabatic compression. Fuselier et al. [2004] proposed that the scattering and  
438 precipitation of  $\sim 50$  keV protons immediately following a large solar wind shock was due to  
439 interactions with electromagnetic ion cyclotron (EMIC) waves. This assumption was later  
440 confirmed by Usanova et al., [2010] who observed EMIC-related precipitation of 30-80 keV  
441 protons on the NOAA POES satellites during enhanced solar wind dynamic pressure. Longdon et  
442 al. [2008] presented observations of riometer absorption following solar wind shocks, and  
443 suggested that enhancements in VLF chorus waves as the driving mechanism.

444 In this study we have presented both EMIC and VLF chorus wave data during the solar wind  
445 shock. The EMIC wave enhancement occurred near simultaneously with the increase in riometer  
446 absorption, whereas the VLF chorus wave enhancement occurred about 5 minutes later.  
447 However, the chorus observations were made on the dawnside and the riometer absorption  
448 observations were made at noon (MLT). Zhou and Tsurutani [1999] found that shock-induced  
449 aurora brighten away from MLT noon at speeds of  $6-11 \text{ km s}^{-1}$ . This suggests that the delay time  
450 of shock effects from noon to dawn could be in the order of 10 minutes, but this is still a factor of  
451 2 longer than observed with the Halley VLF chorus data.

452 Conversely the EMIC wave enhancements were made near MLT noon, and showed no  
453 significant delay compared with the riometer absorption. However the riometer absorption  
454 signature was observed from  $4.8 < L < 13$ , which is inconsistent with the EMIC-driven  
455 precipitation mechanism as this is generally believed to be restricted to inside the plasmapause,  
456 requiring interactions between hot ring current protons and cold plasmaspheric ions to give rise

457 to EMIC wave growth [Fuselier et al., 2004]. Precipitating protons with energies of  $\sim 50$  keV are  
458 unlikely to trigger any response in riometer absorption as they generate excess ionization at  
459 altitudes above at which riometers are sensitive [Turunen et al., 2009; Rodger et al., 2012].

460 The riometer response suggests electron precipitation with energies of  $>30$  keV, and the lack  
461 of any observed response in VLF AARDDVARK data (not shown) suggests electron energies  
462  $<150$  keV. Electron precipitation through the modification of high latitude dayside EMIC waves  
463 [Usanova et al., 2008] is a potential mechanism, as the probability of observing EMIC waves in  
464 space increases during magnetospheric compressions. Anderson et al. [1992] suggested that the  
465 EMIC growth rate peaks at two locations, including at high dayside L-shells ( $5 < L < 11$ ) where the  
466 geomagnetic field is relatively weak as well inside the plasmapause where the cold plasma  
467 density is high. Theoretical study by Summers et al., [1998] suggests that EMIC waves can  
468 interact with MeV electrons via Doppler-shifted cyclotron resonance and cause their  
469 precipitation into the atmosphere. This interaction is possible in extended regions of high plasma  
470 density (like plasmaspheric plumes) but is unlikely to affect 30-150 keV electrons. So far, no  
471 confirmed electron precipitation associated with these high  $L$ -shell dayside EMIC waves has  
472 been reported and the electron energy range is unexpectedly low.

473

#### 474 **4.3 Substorm-injection and precipitation (08:30-11:00 UT)**

475 Clilverd [2008; 2012] combined riometer absorption data and AARDDVARK radio wave data  
476 to estimate the electron precipitation flux occurring during substorms. We undertake the same  
477 calculation here, using the dayside riometer observations from Abisko (11.5 dB), and the  
478 daytime phase and amplitude perturbations:  $+105^\circ / -9$  dB for NRK-SGO, and  $+12^\circ / +2$  dB for  
479 GVT-SGO. The energetic electron precipitation produces mesospheric ionization, and its effects  
480 on VLF wave propagation can be modeled using the Long Wave Propagation Code [LWPC,  
481 Ferguson and Snyder, 1990]. LWPC models VLF signal propagation from any point on Earth to

482 any other point. Given electron density profile parameters for the upper boundary conditions,  
483 LWPC calculates the expected amplitude and phase of the VLF signal at the reception point. A  
484 more detailed description of this technique can be found in Clilverd et al. [2008].

485 Using POES blic flux observations we can calculate the best fit for an energy spectrum e-  
486 folding energy in much the same way as in section 3.3. POES suggests that at the peak of the  
487 substorm precipitation the spectrum can be represented by an e-folding energy of 70 keV. The e-  
488 folding energy compares well with the spectra shown in Figure 6 of Clilverd et al. [2008]. By  
489 using the e-folding energy spectrum value, and sweeping through a range of flux levels, we can  
490 determine the most likely precipitating flux that will give the same results as the observations. In  
491 this case using the riometer absorption target of 11.5 dB we calculate that the substorm >30 keV  
492 flux was  $8.6 \times 10^6$  el.  $\text{cm}^{-2}\text{s}^{-1}\text{sr}^{-1}$ . The >30 keV flux level is about the same as the large substorms  
493 reported in Rodger et al. [2012] who re-modelled the Clilverd et al. [2008; 2012] substorm  
494 fluxes, and slightly less than the flux reported by POES for the same energy range ( $2 \times 10^7$  el.  
495  $\text{cm}^{-2}\text{s}^{-1}\text{sr}^{-1}$  at  $L=7$ , and  $1 \times 10^7$  el.  $\text{cm}^{-2}\text{s}^{-1}\text{sr}^{-1}$  at  $L=6$ ) in this event.

496 However, when using the e-folding spectrum and the flux required to model the riometer  
497 observations we found that we were unable to reproduce the changes in the VLF propagation  
498 conditions, particularly the Iceland- Sodankylä path (NRK-SGO) using the LPWC. This path is  
499 quasi-constant at  $L=5-6$ , and should be representative of the centre of the precipitation region  
500 during the substorm [Berkey et al, 1974]. Clilverd et al. [2008] found that they required a non e-  
501 folding spectrum to accurately model VLF propagation conditions, and instead used spectral  
502 information from the LANL-97A geostationary satellite which showed much higher fluxes at  
503 higher energies than a typical 50 keV e-folding spectrum would suggest, particularly at energies  
504 >400 keV (see Figure 6 of that study). In Clilverd et al. [2010] a fit was made to DEMETER  
505 electron spectra from ~90-700 keV in terms of a power law where the slope (scaling exponent,  $k$ )  
506 typically ranged from -1 to -3. A power law slope of  $k=-3$  represents the LANL-97A substorm

507 spectra in Clilverd et al. [2008], and in our current study is able to reproduce both the VLF  
508 propagation changes shown by NRK-SGO during the 09 UT substorm, and the peak riometer  
509 absorption value of 11.5 dB, using a  $>30$  keV flux of  $1.35 \times 10^7$  el.  $\text{cm}^{-2}\text{s}^{-1}\text{sr}^{-1}$ . This  $>30$  keV  
510 EEP flux magnitude value is similar to the e-folding flux, and similar to the  $>30$  keV blc flux  
511 levels observed by POES. In contrast with the 05-08 UT wave-driven event discussed in section  
512 4.1, there is no difference in the experimentally estimated flux and the POES-observed blc  
513 fluxes, whereas the wave-driven event suggested a factor of  $\sim 30$  difference. This could be  
514 explained by different pitch angle distributions within the blc, driven by strong or weak diffusion  
515 for the various processes. Strong diffusion would be more likely to isotropically fill the loss  
516 cone, and produce a smaller conversion factor for the POES observations. Thus we suggest that  
517 substorms have pitch angle distribution that is consistent with an isotropically-filled loss cone,  
518 while the wave-driven precipitation event has the characteristics of a weak diffusion process  
519 [Kennel and Petschek, 1966].

520 Figure 9 shows the similarities and differences of the 70 keV e-folding spectrum (red lines)  
521 and the  $k=-3$  spectrum (blue lines) which both reproduce the Abisko-reported riometer  
522 absorptions. The left-hand panel shows how the electron integral flux density varies with  
523 electron energy over the range 10 keV to 3 MeV. The black crosses represent the  $>30$ ,  $>100$ ,  
524  $>300$  keV blc fluxes measured by POES at the peak of the substorm. It is clear that using POES  
525 data alone, the spectrum can be well represented by either e-folding, or power law characteristics  
526 but there are only three energy ranges to constrain the spectral fitting. Both spectra give the same  
527 riometer absorption value, and only the addition of the AARDDVARK observations and  
528 modeling can differentiate between the two. Xiao et al. [2008 and references therein] showed  
529 that fits to the energy spectrum of trapped electron measurements from the LANL satellites are  
530 best described by a kappa-type (KT) power law index. In the energy range considered in this  
531 study the kappa-type distributions shown in Xiao et al. [2008] closely resemble our  $k=-3$  spectral

532 gradient and lend weight to the use of a power-law energy spectrum to model the EEP events.  
533 The right-hand panel shows the calculated altitude dependent electron number density as a result  
534 of precipitating electrons with the two different spectra. The solid black line represents the non-  
535 disturbed ionosphere during daytime in the region of Abisko in April 2010. The ambient  
536 ionospheric profile is determined using a Wait nighttime profile up to 85 km, and an IRI profile  
537 above [following Rodger et al., 2012]. Although the  $>30$  keV flux is similar for both spectra, the  
538  $k=-3$  line shows higher fluxes  $>500$  keV, and the 70 keV e-folding line shows higher fluxes for  
539  $\sim 100$ -300 keV. The effect on the ionosphere when these spectra precipitate is for greater  
540 ionization at low altitudes ( $\sim 50$  km) and at high altitudes ( $\sim 100$  km) for the  $k=-3$  spectra, while  
541 the 70 keV e-folding spectra produces higher electron number density at  $\sim 70$  km. This altitude  
542 difference can be significant in terms of chemical changes caused by the ionization, the lifetime  
543 of the species produced, and their impact on the neutral atmosphere [Brasseur and Solomon,  
544 1995].

545

## 546 **5. Summary**

547 On the 5<sup>th</sup> April 2010 a CME-driven solar wind shock compressed the Earth's  
548 magnetosphere, and induced an operational anomaly in the Galaxy 15 geosynchronous  
549 communications satellite [Allen, 2010]. The shock arrived at the Earth at 08:25 UT. In this  
550 study we have described the energetic electron precipitation throughout the Galaxy 15 period,  
551 including the characteristics observed before the arrival of the solar wind shock event, during  
552 the shock itself, and as a result of the large substorm injection shortly after the shock.

553 Prior to the solar wind shock a period of negative IMF Bz gave rise to a period of geomagnetic  
554 disturbance during which electron acceleration occurred, consistent with the presence of chorus  
555 waves that were observed on the dawnside. Electron acceleration and loss was observed at the  
556 same time, with the precipitation of electrons into the atmosphere occurring primarily on the

557 dayside of the Earth. Using POES integral b/c fluxes for >30, >100, and >300 keV we calculate  
558 that the e-folding energy of the precipitating electron spectrum to be 55 keV, with peak fluxes of  
559  $1.7 \times 10^6$  el.  $\text{cm}^{-2}\text{s}^{-1}\text{sr}^{-1}$  in order to reproduce the Abisko 3.5 dB absorption observed. The  
560 dayside energetic electron precipitation, identified by riometer absorption enhancements, was  
561 confined to  $L$ -shells outside of the plasmapause, which is consistent with the likely inner  
562 boundary of the chorus region. Although the POES b/c >100 keV fluxes increased by a factor of  
563 40 during the event, the calculated fluxes on the basis of the ground-based observations were a  
564 factor of 30 times larger again. This is consistent with the idea that some adjustment needs to be  
565 made to the POES b/c fluxes to take into account the orientation of the telescope to the b/c, and  
566 the non-isotropic distribution of electrons within the b/c. The observations suggest that the  
567 chorus-wave event produced energetic electron precipitation via a weak diffusion process.

568 During the solar wind shock, a few minutes of 30-150 keV electron precipitation was observed  
569 on the dayside, and over a large  $L$ -shell range ( $4.8 < L < 13$ ). The timing of the pulse was consistent  
570 with the enhancement of EMIC waves in the range 0.25-1 Hz on the dayside, whereas enhanced  
571 VLF chorus waves were only observed 5 minutes later. Adiabatic magnetospheric compression  
572 leading to loss cone instability, wave growth, and enhanced pitch angle scattering is likely to  
573 have taken place, but the low energy of precipitating electrons and the high geomagnetic latitude  
574 of the precipitation suggests that interaction with EMIC waves in high cold density regions is  
575 unlikely to have played a role. High latitude dayside EMIC waves may have caused the  
576 enhanced pitch angle scattering, but further work is required to identify the mechanism  
577 conclusively.

578 The electron precipitation fluxes driven by the substorm injection occurring shortly after the  
579 shock arrival were estimated using riometer and AARDDVARK subionospheric VLF wave  
580 propagation observations. Riometer absorption levels of  $\sim 11$  dB during the substorm represent  
581 an extreme event, although the estimated fluxes were roughly the same level as other large

582 substorm events previously analyzed. The  $>30$  keV fluxes were found to be  $1.35 \times 10^7$  el.  $\text{cm}^{-2}\text{s}^{-1}$   
583  $\text{sr}^{-1}$  which was consistent with those observed by the POES blc telescopes, and suggest an  
584 isotropically filled blc. However using POES to estimate the energy spectrum of the substorm-  
585 driven electron precipitation gave an e-folding energy spectrum of 70 keV, but the observed  
586 AARDDVARK responses suggest that an e-folding energy spectrum would underestimate the  
587 higher ( $>400$  keV) electron fluxes. Instead, a power law spectrum is more appropriate, with a  
588 scaling factor of  $k=-3$ .

589 In summary, a few hours prior to the Galaxy 15 anomaly electron acceleration at  $>0.6$  MeV,  
590 took place in the region of the Galaxy 15 satellite on the nightside. Then, an hour prior to the  
591 anomaly, a solar wind shock event generated a few minutes of 30-150 keV electron precipitation,  
592 possibly associated with EMIC waves, but was observed only on the dayside over a large  $L$ -shell  
593 range ( $4.8 < L < 13$ ). Finally, a substorm injection event was triggered by the shock, and appears to  
594 have ultimately triggered the upset on Galaxy 15. However, we have shown that the peak  
595  $>30$  keV electron precipitation fluxes of  $1.35 \times 10^7$  el.  $\text{cm}^{-2}\text{s}^{-1}\text{sr}^{-1}$  were only about the same level  
596 as other large substorm events previously analyzed, indicating either a sensitivity to the energetic  
597 electron environment prior to the event, or that the satellite was in a vulnerable situation.

598

599

600 **Acknowledgments.** The authors would like to acknowledge the support of the Australian  
601 Antarctic Division project number: ASAC 1324 for the Casey data. We would also like to  
602 acknowledge the use of the AAD data system for the provision of the Macquarie Island  
603 Riometer data, [http://www.ips.gov.au/World\\_Data\\_Centre/1/8](http://www.ips.gov.au/World_Data_Centre/1/8). The Scott Base experiment is  
604 supported by Antarctica New Zealand, event number K060. MU is funded by the Canadian  
605 Space Agency. The research leading to these results has received funding from the

606 European Union Seventh Framework Programme [FP7/2007-2013] under grant  
607 agreement n°263218. CJR was supported by the New Zealand Marsden Fund.

608

609

610

## 611 **References**

612 Allen, J. (2010), The Galaxy 15 Anomaly: Another Satellite in the Wrong Place at a Critical  
613 Time, *Space Weather*, 8, 2, doi:10.1029/2010SW000588.

614

615 Anderson, B. J., R. E. Erlandson, and L. J. Zanetti (1992), A statistical study of Pc 1–2  
616 magnetic pulsations in the equatorial magnetosphere: 1. Equatorial occurrence distribution, *J.*  
617 *Geophys. Res.*, 97, 3075–3088.

618

619 Andersson, M., P. T. Verronen, S. Wang, C. J. Rodger, M. A. Clilverd, and B. R. Carson (2012),  
620 Precipitating radiation belt electrons and the production of mesospheric hydroxyl during 2004–  
621 2009, *J. Geophys. Res.*, doi:10.1029/2011JD01724, (in press).

622

623 Barr, R., D. L. Jones, and C. J. Rodger (2000), ELF and VLF radio waves, *J. Atmos. Sol.-Terr.*  
624 *Phys.*, 62, 1689-1718.

625

626 Berkey, F. T., V. M. Driatskiy, K. Henriksen, B. Hultqvist, D. H. Jelly, T. I. Shchuka, A.  
627 Theander, and J. Yliniemi (1974), A synoptic investigation of particle precipitation dynamics  
628 for 60 substorms in IQSY (1964–1965) and IASY (1969), *Planet. Space Sci.*, 22, 255–307.

629

630 Brasseur, G., and S. Solomon (2005), *Aeronomy of the Middle Atmosphere*, third ed., D. Reidel  
631 Publishing Company, Dordrecht.

632

633 Clilverd, M. A., C. J. Rodger, and T. Ulich (2006), The importance of atmospheric precipitation  
634 in storm-time relativistic electron flux drop outs, *Geophys. Res. Lett.*, 33, L01102,  
635 doi:10.1029/2005GL024661.

636

637 Clilverd, M. A., C. J. Rodger, R. M. Millan, J. G. Sample, M. Kokorowski, M. P. McCarthy, T.  
638 Ulich, T. Raita, A. J. Kavanagh, and E. Spanswick (2007), Energetic particle precipitation into  
639 the middle atmosphere triggered by a coronal mass ejection, *J. Geophys. Res.*, 112, A12206,  
640 doi:10.1029/2007JA012395.

641

642 Clilverd, M. A., C. J. Rodger, J. B. Brundell, N. Cobbett, J. Bähr, T. Moffat-Griffin, A. J.  
643 Kavanagh, A. Seppälä, N. R. Thomson, R. H. W. Friedel, and F. W. Menk (2008), Energetic  
644 electron precipitation during sub-storm injection events: high latitude fluxes and an  
645 unexpected mid-latitude signature, *J. Geophys. Res.*, 113, A10311, doi: 10.1029/  
646 2008JA013220.

647

648 Clilverd, M. A., C. J. Rodger, N. R. Thomson, J. B. Brundell, Th. Ulich, J. Lichtenberger, N.  
649 Cobbett, A. B. Collier, F. W. Menk, A. Seppälä, P. T. Verronen, and E. Turunen (2009),  
650 Remote sensing space weather events: the AARDDVARK network, *Space Weather*, 7,  
651 S04001, doi: 10.1029/2008SW000412.  
652

653 Clilverd, M. A., C. J. Rodger, R. J. Gamble, Th. Ulich, T. Raita, A. Seppälä, J. C. Green, N. R.  
654 Thomson, J.-A. Sauvaud, and M. Parrot (2010), Ground-based estimates of outer radiation belt  
655 energetic electron precipitation fluxes into the atmosphere, *J. Geophys. Res.*, 115, A12304,  
656 doi: 10.1029/2010JA015638.  
657

658 Clilverd, M. A., C. J. Rodger, I. J. Rae, J. B. Brundell, N. R. Thomson, N. Cobbett, P. T.  
659 Verronen, and F. W. Menk (2012), Combined THEMIS and ground-based observations of a  
660 pair of substorm associated electron precipitation events, *J. Geophys. Res.*, 117, A02313,  
661 doi:10.1029/2011JA016933.  
662

663 Connors, M., C. T. Russell, and V. Angelopoulos (2011), Magnetic flux transfer in the 5 April  
664 2010 Galaxy 15 substorm: an unprecedented observation, *Ann. Geophys.*, 29, 619-622,  
665 doi:10.5194/angeo-29-619-2011.  
666

667 Erlandson, R. E., K. Mursula, and T. Bösinger (1996), Simultaneous ground-satellite  
668 observations of structured Pc 1 pulsations, *J. Geophys. Res.*, 101(A12), 27,149–27,156,  
669 doi:10.1029/96JA02645.  
670

671 Evans, D. S., and M. S. Greer (2004), Polar orbiting environmental satellite space environment  
672 monitor - 2 instrument descriptions and archive data documentation, NOAA technical  
673 Memorandum version 1.4, Space Environment Laboratory, Colorado.  
674

675

676 Ferguson, J. A., and F. P. Snyder (1990), Computer programs for assessment of long wavelength  
677 radio communications, Tech. Doc. 1773, Natl. Ocean Syst. Cent., San Diego, California.  
678

679 Fok, M.-C., R. B. Horne, N. P. Meredith, and S. A. Glauert (2008), Radiation Belt Environment  
680 Model: Application to space weather nowcasting, *J. Geophys. Res.*, 113, A03S08,  
681 doi:10.1029/2007JA012558.  
682

683 Fuselier, S. A., S. P. Gary, M. F. Thomsen, E. S. Claflin, B. Hubert, B. R. Sandel, and T. Immel  
684 (2004), Generation of transient dayside subauroral proton precipitation, *J. Geophys. Res.*, 109,  
685 A12227, doi:10.1029/2004JA010393.  
686

687 Hendry, A. T., C. J. Rodger, M. A. Clilverd, N. R. Thomson, S. K. Morley, and T. Raita (2012),  
688 Rapid radiation belt losses occurring during high speed solar wind stream driven storms:  
689 importance of energetic electron precipitation, *American Geophysical Union Monograph on*  
690 *"Dynamics of the Earth's Radiation Belts and Inner Magnetosphere"* edited by D Summers, I R  
691 Mann, D N Baker, and M Schulz, (in press), doi:10.1029/2012BK001299.  
692

693 Horne, R.B. (2002), The contribution of wave-particle interactions to electron loss and  
694 acceleration in the Earth's radiation belts during geomagnetic storms, in *URSI Review of Radio*  
695 *Science 1999-2002*, edited by W.R. Stone, pp. 801-828, Wiley.  
696

697 Horne R. B., R. M. Thorne, S. A. Glauert, J. M. Albert, N. P. Meredith, R. R. Anderson (2005),  
698 Timescale for radiation belt electron acceleration by whistler mode chorus waves, *J. Geophys.*  
699 *Res.*, 110, A03225, doi:10.1029/2004JA010811.  
700

701 Kangas, J., A. Aikio, and J. V. Olson (1986), Multistation correlation of ULF pulsations spectra  
702 associated with sudden impulses, *Planet. Space Sci.*, **34**, 543-.  
703

704 Kennel, C. F., and H. E. Petschek (1966), Limit on stably trapped particle fluxes, *J. Geophys.*  
705 *Res.*, 71, 1-28.  
706

707 Lam, M. M., R. B. Horne, N. P. Meredith, S. A. Glauert, T. Moffat-Griffin, and J. C. Green  
708 (2010), Origin of energetic electron precipitation >30 keV into the atmosphere, *J. Geophys.*  
709 *Res.*, 115, A00F08, doi:10.1029/2009JA014619.  
710

711 Larsen, T. R., and G. R. Thomas (1974), Energy spectra measured during a relativistic electron  
712 precipitation event on 2 February 1969, *J. Atmos. Terr. Phys.*, 36, 1613-1622.  
713

714 Little, C.G. and H. Leinbach (1959), The riometer: a device for the continuous measurements of  
715 ionospheric absorption, *Proc. IRE*, 37, 315-320.  
716

717 Longden, N., M. H. Denton, and F. Honary (2008), Particle precipitation during ICME-driven  
718 and CIR-driven geomagnetic storms, *J. Geophys. Res.*, 113, A06205,  
719 doi:10.1029/2007JA012752.  
720

721 Miyoshi, Y., K. Sakaguchi, K. Shiokawa, D. Evans, J. Albert, M. Connors, and V. Jordanova  
722 (2008), Precipitation of radiation belt electrons by EMIC waves, observed from ground and  
723 space, *Geophys. Res. Lett.*, 35, L23101, doi:10.1029/2008GL035727.  
724

725 Ni, B., R. M. Thorne, Y. Y. Shprits, K. G. Orlova, and N. P. Meredith (2011), Chorus-driven  
726 resonant scattering of diffuse auroral electrons in nondipolar magnetic fields, *J. Geophys. Res.*,  
727 116, A06225, doi:10.1029/2011JA016453.  
728

729 Onsager, T. G., R. Grubb, J. Kunches, L. Matheson, D. Speich, R. Zwickl, and H. Sauer (1996),  
730 Operational uses of the GOES energetic particle detectors, in *GOES-8 and Beyond: 7 – 9*  
731 *August 1996, Denver, Colorado*, edited by E. R. Washwell, *Proc. SPIE Int. Soc. Opt. Eng.*,  
732 2812, 281.  
733

734 Randall, C. E., et al. (2005), Stratospheric effects of energetic particle precipitation in 2003–  
735 2004, *Geophys. Res. Lett.*, 32, L05802, doi:10.1029/2004GL022003.  
736

737 Reeves, G. D., et al., (2003), Acceleration and loss of relativistic electrons during geomagnetic  
738 storms, *Geophys. Res. Lett.*, vol. 30(10), 1529, doi:10.1029/2002GL016513.  
739

740 Rodger, C. J., O. A. Molchanov, and N. R. Thomson (1998), Relaxation of transient ionization in  
741 the lower ionosphere, *J. Geophys. Res.*, 103(4), 6969-6975.  
742

743 Rodger, C. J., M. A. Clilverd, N. R. Thomson, R. J. Gamble, A. Seppälä, E. Turunen, N. P.  
744 Meredith, M. Parrot, J. A. Sauvaud, and J.-J. Berthelier (2007a), Radiation belt electron

745 precipitation into the atmosphere: recovery from a geomagnetic storm, *J. Geophys. Res.*, 112,  
746 A11307, doi: 10.1029/2007JA012383.

747

748 Rodger, C. J., M. A. Clilverd, D. Nunn, P. T. Verronen, J. Bortnik, E. Turunen (2007b), Storm  
749 time, short-lived bursts of relativistic electron precipitation detected by subionospheric radio  
750 wave propagation, *J. Geophys. Res.*, 112, A07301, doi: 10.1029/2007JA012347.

751

752 Rodger, C. J., T. Raita, M. A. Clilverd, A. Seppälä, S. Dietrich, N. R. Thomson, and Th. Ulich  
753 (2008a), Observations of relativistic electron precipitation from the radiation belts driven by  
754 EMIC Waves, *Geophys. Res. Lett.*, 35, L16106, doi: 10.1029/2008GL034804.

755

756 Rodger, C. J., and M. A. Clilverd (2008b), Magnetospheric physics: Hiss from the chorus,  
757 *Nature*, 452 (7183), 41-42, doi:10.1038/452041a.

758

759 Rodger, C. J., M. A. Clilverd, J. Green, and M.-M. Lam (2010a), Use of POES SEM-2  
760 observations to examine radiation belt dynamics and energetic electron precipitation in to the  
761 atmosphere, *J. Geophys. Res.*, 115, A04202, doi: 10.1029/2008JA014023.

762

763 Rodger, C. J., M. A. Clilverd, A. Seppälä, N. R. Thomson, R. J. Gamble, M. Parrot, J.-A.  
764 Sauvaud and Th. Ulich (2010b), Radiation belt electron precipitation due to geomagnetic  
765 storms: significance to middle atmosphere ozone chemistry, *J. Geophys. Res.*, 115, A11320,  
766 doi: 10.1029/2010JA015599.

767

768 Rodger, C J, B R Carson, S A Cummer, R J Gamble, M A Clilverd, J-A Sauvaud, M Parrot, J C  
769 Green, and J-J Berthelier (2010c), Contrasting the efficiency of radiation belt losses caused by  
770 ducted and non-ducted whistler mode waves from ground-based transmitters, *J. Geophys.*  
771 *Res.*, 115, A12208, doi:10.1029/2010JA015880.

772

773 Rodger, C. J., M. A. Clilverd, A. J. Kavanagh, C. E. J. Watt, P. T. Verronen, and T. Raita (2012),  
774 Contrasting the responses of three different ground-based instruments to energetic electron  
775 precipitation, *Radio Sci.*, 47(2), RS2021, doi:10.1029/2011RS004971.

776

777 Seppälä, A, M. A. Clilverd, and C. J. Rodger (2007), NO<sub>x</sub> enhancements in the middle  
778 atmosphere during 2003-2004 polar winter: Relative significance of solar proton events and  
779 the aurora as a source, *J. Geophys. Res.*, D23303, doi: 10.1029/2006JD008326.

780

781 Seppälä, A., C. E. Randall, M. A. Clilverd, E. Rozanov, and C. J. Rodger (2009), Geomagnetic  
782 activity and polar surface level air temperature variability, *J. Geophys. Res.*, 114, A10312, doi:  
783 10.1029/2008JA014029.

784

785 Smith, A.J. (1995), VELOX: a new VLF/ELF receiver in Antarctica for the Global Geospace  
786 Science mission, *Journal of Atmospheric and Terrestrial Physics* 57, 507–524.

787

788 Smith, A.J., R.B.Horne, N.P.Meredith (2010), The statistics of natural ELF/VLF waves derived  
789 from a long continuous set of ground-based observations at high latitude, *Journal of*  
790 *Atmospheric and Solar-Terrestrial Physics*, 72, 463–475.

791

792 Spann, J. F., M. Brittnacher, R. Elsen, G. A. Germany, and G. K. Parks (1998), Initial response  
793 and complex polar cap structures of the aurora in response to the January 10, 1997 magnetic  
794 cloud, *Geophys. Res. Lett.*, 25, 2577.  
795

796 Spanswick, E., et al. (2009), Global observations of substorm injection region evolution: 27  
797 August 2001, *Ann. Geophys.*, 27, 2019-2025.  
798

799 Summers, D., R. M. Thorne, and F. Xiao (1998), Relativistic theory of wave-particle resonant  
800 diffusion with application to electron acceleration in the magnetosphere, *J. Geophys. Res.*,  
801 103(A9), 20,487–20,500, doi:10.1029/98JA01740.  
802

803 Tsurutani, B. T., et al., (2001), Auroral zone dayside precipitation during magnetic  
804 storm initial phases, *J. Atmos. Sol. Terr. Phys.*, 63, 513.  
805

806 Turunen, E., P. T. Verronen, A. Seppälä, C. J. Rodger, M. A. Clilverd, J. Tamminen, C. F. Enell  
807 and Th. Ulich (2009), Impact of different precipitation energies on NO<sub>x</sub> generation during  
808 geomagnetic storms, *J. Atmos. Sol.-Terr. Phys.*, 71, pp. 1176-1189,  
809 doi:10.1016/j.jastp.2008.07.005.  
810

811 Usanova (2008) Usanova, M. E., I. R. Mann, I. J. Rae, Z. C. Kale, V. Angelopoulos, J. W.  
812 Bonnell, K.-H. Glassmeier, H. U. Auster, and H. J. Singer (2008), Multipoint observations of  
813 magnetospheric compression-related EMIC Pc1 waves by THEMIS and CARISMA, *Geophys*  
814 *Res Lett.*, 35, L17S25, doi:10.1029/2008GL034458.  
815

816 Usanova, M. E., et al. (2010), Conjugate ground and multisatellite observations of  
817 compression-related EMIC Pc1 waves and associated proton precipitation, *J. Geophys. Res.*,  
818 115, A07208, doi:10.1029/2009JA014935.  
819

820 Verronen, P. T., C. J. Rodger, M. A. Clilverd, and S. Wang (2011), First evidence of  
821 mesospheric hydroxyl response to electron precipitation from the radiation belts, *J. Geophys.*  
822 *Res.*, 116, D07307, doi: 10.1029/2010JD014965.  
823

824 Xiao, F., R. M. Thorne, and D. Summers (2007), Higher-order gyroresonant acceleration of  
825 electrons by superluminous (AKR) wave-modes, *Planet. Space Sci.*, 55, 1257.  
826

827 Xiao, F., C. Shen, Y. Wang, H. Zheng, and S. Wang (2008), Energetic electron distributions  
828 fitted with a relativistic kappa-type function at geosynchronous orbit, *J. Geophys. Res.*, 113,  
829 A05203, doi:10.1029/2007JA012903.  
830

831 Xiao, F., Z. Su, H. Zheng, and S. Wang (2010), Three-dimensional simulations of outer radiation  
832 belt electron dynamics including cross-diffusion terms, *J. Geophys. Res.*, 115, A05216,  
833 doi:10.1029/2009JA014541.  
834

835 Xiao, F., S. Zhang, Z. Su, Z. He, and L. Tang (2012), Rapid acceleration of radiation belt  
836 energetic electrons by Z-mode waves, *Geophys. Res. Lett.*, 39, L03103,  
837 doi:10.1029/2011GL050625.  
838

839 Zhou, X.-Y., and B. T. Tsurutani, Rapid intensification and propagation of the dayside aurora:  
840 Large-scale interplanetary pressure pulses (fast shocks), *Geophys. Res. Lett.*, 26, 1097, 1999.

841  
842 Zhou, X.-Y., R. J. Strangeway, P. C. Anderson, D. G. Sibeck, B. T. Tsurutani, G. Haerendel, H.  
843 U. Frey, and J. K. Arballo, Shock aurora: FAST and DMSP observations, *J. Geophys. Res.*,  
844 108(A4), 8019, doi:10.1029/2002JA009701, 2003.

845  
846 \_\_\_\_\_  
847  
848 M. A. Clilverd, British Antarctic Survey (NERC), High Cross, Madingley Road, Cambridge CB3 0ET, England, U.K. (email:  
849 [macl@bas.ac.uk](mailto:macl@bas.ac.uk))

850  
851 D. Danskin, Geomagnetic Laboratory, Natural Resources Canada, Ottawa, Canada. (email: [Donald.Danskin@NRCan-](mailto:Donald.Danskin@NRCan-RNCan.gc.ca)  
852 [RNCan.gc.ca](mailto:Donald.Danskin@NRCan-RNCan.gc.ca))

853  
854 C. J. Rodger, Department of Physics, University of Otago, P.O. Box 56, Dunedin, New Zealand. (email:  
855 [crodger@physics.otago.ac.nz](mailto:crodger@physics.otago.ac.nz))

856  
857 T. Raita, and Th. Ulich, Sodankylä Geophysical Observatory, University of Oulu, Sodankylä, Finland. (email:  
858 [tero.raita@sgo.fi](mailto:tero.raita@sgo.fi) [th.ulich@sgo.fi](mailto:th.ulich@sgo.fi) )

859  
860 E. L. Spanswick, Dept. of Physics and Astronomy, University of Calgary, 2500 University Drive, Calgary, Alberta,  
861 Canada T2N 1N4 (email: [emma@phys.ucalgary.ca](mailto:emma@phys.ucalgary.ca) )

862  
863 M. E. Usanova, Department of Physics, University of Alberta, Edmonton, AB T6G 2A1, Canada. (email:  
864 [musanova@ualberta.ca](mailto:musanova@ualberta.ca))

865  
866

867 (Received N x, 2012; N x 27, 2012;

868 accepted N x, 2012.)

869

870 CLILVERD ET AL.: GALAXY 15 ELECTRON PRECIPITATION

871

872 **Figures**

873 **Figure 1.** The geomagnetic conditions on 05 April 2010, 00-12 UT. From top to  
874 bottom the panels show the variation of the solar wind speed and density, the IMF Bz  
875 component, and the AE (positive values) and AO (negative values) geomagnetic  
876 index variations. The panels indicate that predominantly negative Bz existed during  
877 most of the study period, with moderate to severe geomagnetic disturbance levels  
878 occurring at ~06 UT and ~09 UT. The ~09 UT disturbance was initiated by a sudden  
879 solar wind shock at ~08:25 UT.

880 **Figure 2.** An indication of the MLT positions of the observation sites discussed in  
881 this study at 06 UT (left panel) and 09 UT (right panel) on 05 April 2010.

882 **Figure 3.** A plot indicating the satellite and ground-based observations that were  
883 made during the 00-12 UT period on 05 April 2010. Similarities can be seen in the  
884 variation of GOES-11 (>0.6 MeV and >2 MeV electrons), POES (>100 keV  
885 ‘trapped’ and ‘blc’ electrons) and the Abisko riometer absorption at ~06 UT, and  
886 ~09 UT.

887 **Figure 4.** Upper panel. The Halley VELOX data, 00-12 UT, 05 April 2010. VLF  
888 wave intensity from 0.5-10 kHz are shown (units of  $\text{dB} > 10^{-33} \text{ T}^2 \text{ Hz}^{-1}$ ). The electron  
889 gyrofrequency ( $f_{ce}$ ) at the L-shell of Halley is ~10 kHz, corresponding to the top of  
890 the panel.. Enhanced wave activity at ~2 kHz can be observed at ~05 UT, lasting  
891 until ~08 UT, followed by a sudden enhancement at ~1 kHz at 08:25 UT, as well as  
892 the appearance of ~6 kHz waves at ~09-10 UT. Lower panel. The Rovaniemi Pc 1-2  
893 wave power over the same period. EMIC waves are observed following the solar  
894 wind compression at 08:25 UT.

895 **Figure 5.** Observations during the period from 04:00-08:24 UT, with the upper two  
896 panels containing GOES >600 keV and >2 MeV fluxes respectively. The two

897 riometer panels show nightside Macquarie Island absorption, and dayside Abisko  
898 absorption variations respectively, while the penultimate panel shows the dawnside  
899 VLF 2.0 kHz wave intensity at Halley, Antarctica.

900 **Figure 6:** Top to bottom panels. The GOES >600 keV fluxes, Macquarie Island  
901 riometer absorption, Rovaniemi Pc 1-2 wave intensity, Abisko riometer absorption,  
902 and Halley VLF wave intensity from 08:15 to 08:54 UT. The time of the shock  
903 arrival is indicated by the vertical dashed line. The approximate MLT sector of the  
904 measurements is indicated for each panel.

905 **Figure 7:** Left panel. The >300 keV b/c flux as a function of UT and  $L$ -shell. The  
906 Galaxy 15 substorm can be seen as a sudden increase in flux just after 09 UT, spread  
907 over a large range of  $L$ -shell ( $L=4-11$ ). Right hand panel. The substorm impact on  
908 riometers on the nightside (Macquarie Island and Dawson) as well as on the dayside  
909 (Abisko). An approximate onset time of the substorm is indicated by the vertical  
910 dotted line at 08:55 UT.

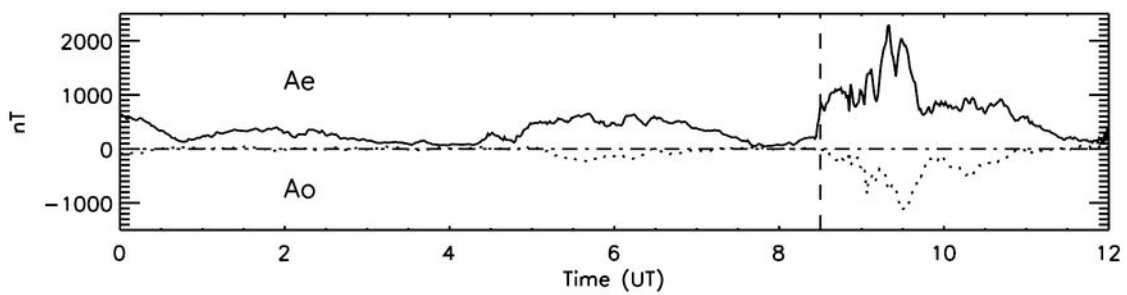
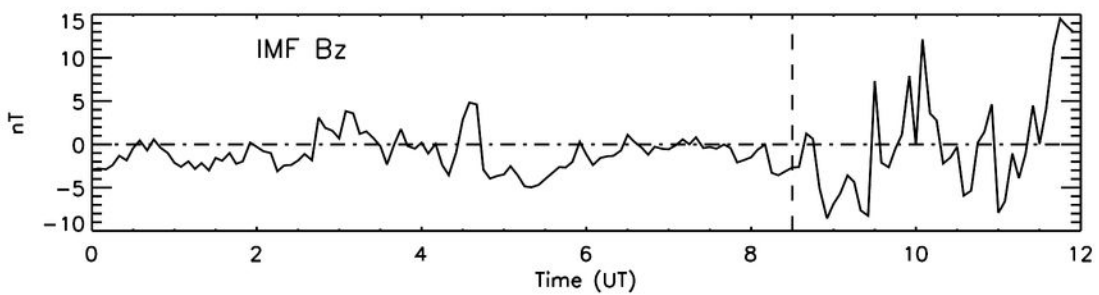
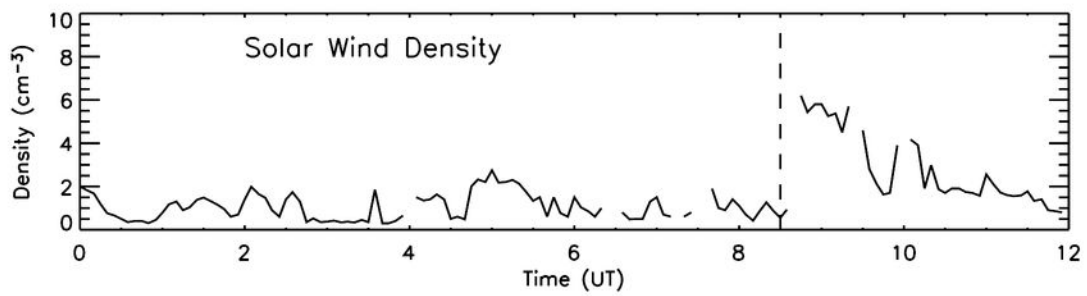
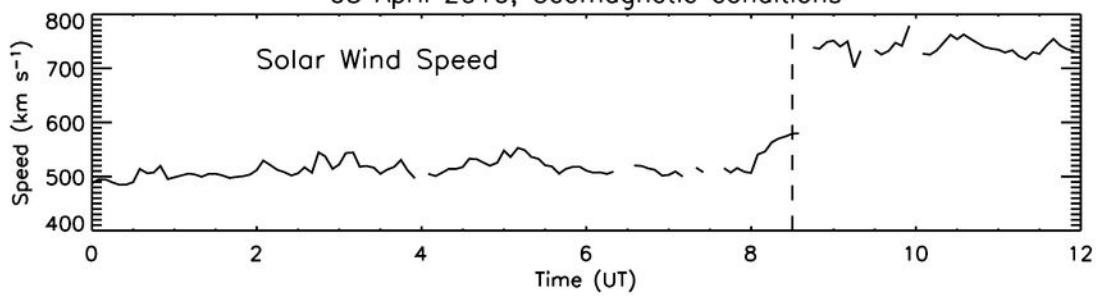
911 **Figure 8:** Upper panel. AARDDVARK data received at Sodankylä during 5<sup>th</sup> May  
912 2010, Iceland-Sodankylä (NRK-SGO, 37.5 kHz,  $L\sim 5-6$ ), and UK-Sodankylä (GVT-  
913 SGO, 22.1 kHz,  $2.5 < L < 5.3$ ). Both phase (dashed lines) and amplitude (solid line) are  
914 shown for each transmitter-receiver path, with the approximate substorm onset time  
915 shown by a vertical dotted line. The lower panel shows AARDDVARK data from  
916 two transmitters received at Antarctic stations on the nightside, Hawaii-Casey (NPM-  
917 CAS, 21.4 kHz,  $1 < L < 999$ ), and North Dakota-Scott Base (NDK-SB, 25.2 kHz,  
918  $1 < L < 32$ ).

919 **Figure 9:** Left-hand panel. Electron integral flux density varying with electron  
920 energy over the range 10 keV to 3 MeV, for a 70 keV e-folding spectra (red line) and  
921 a  $k=-3$  power law spectra (blue line). The black crosses represent the >30, >100,

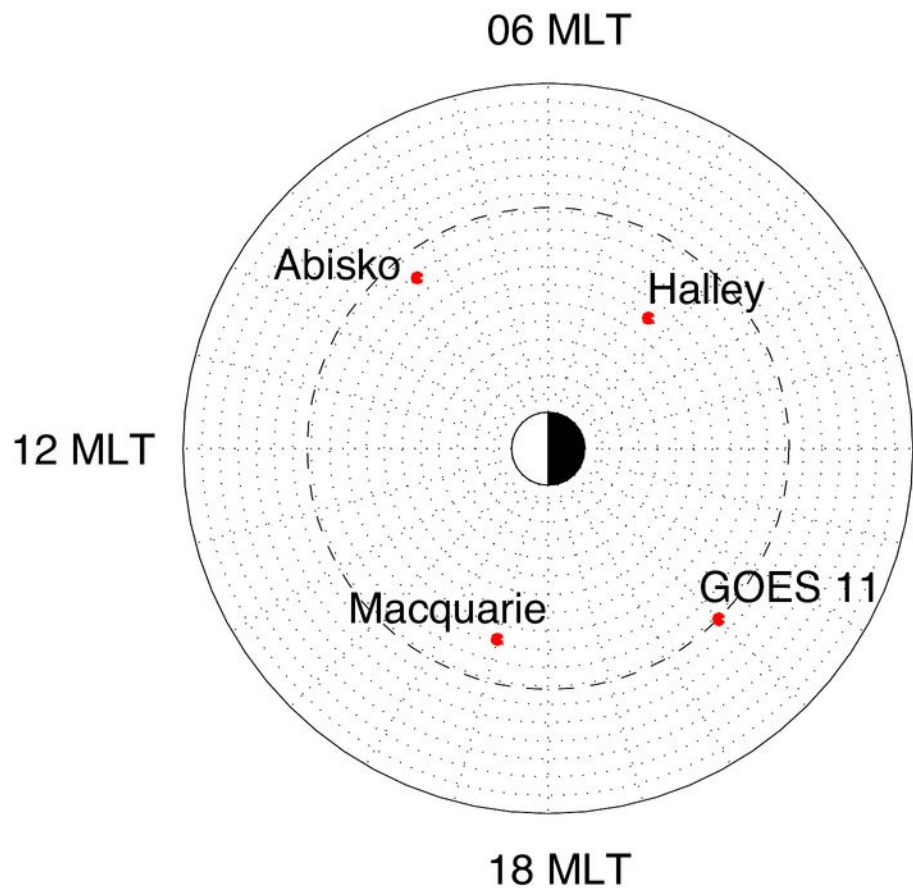
922 >300 keV b/c fluxes measured by POES at the peak of the substorm. Right-hand  
923 panel. The calculated altitude dependent electron number density as a result of  
924 precipitating electrons with the two spectra. The solid black line represents the non-  
925 disturbed ionosphere during daytime in the region of Abisko in April 2010. The  
926 ambient ionospheric profile is determined using a Wait nighttime profile up to 85  
927 km, and an IRI profile above – see text for more details.

928

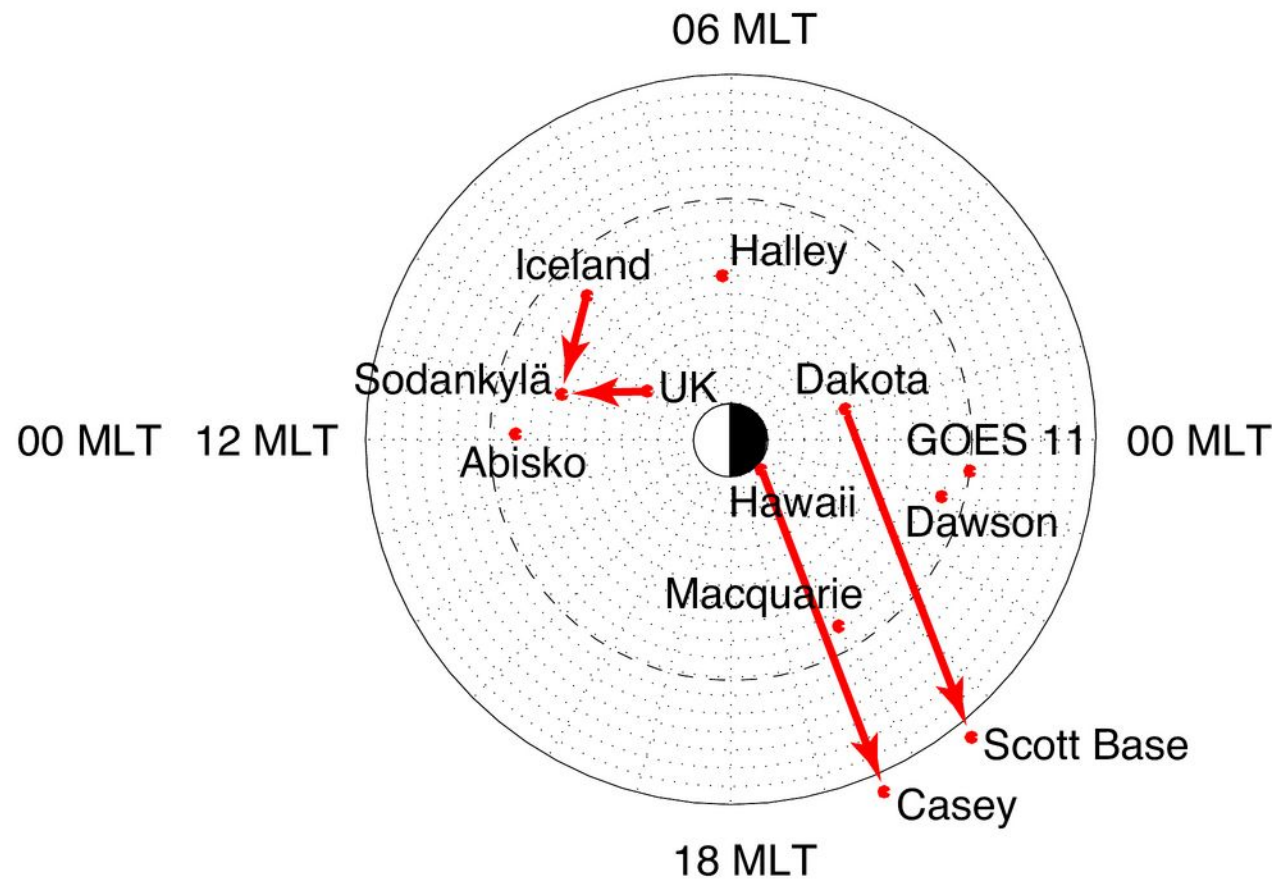
05 April 2010, Geomagnetic conditions



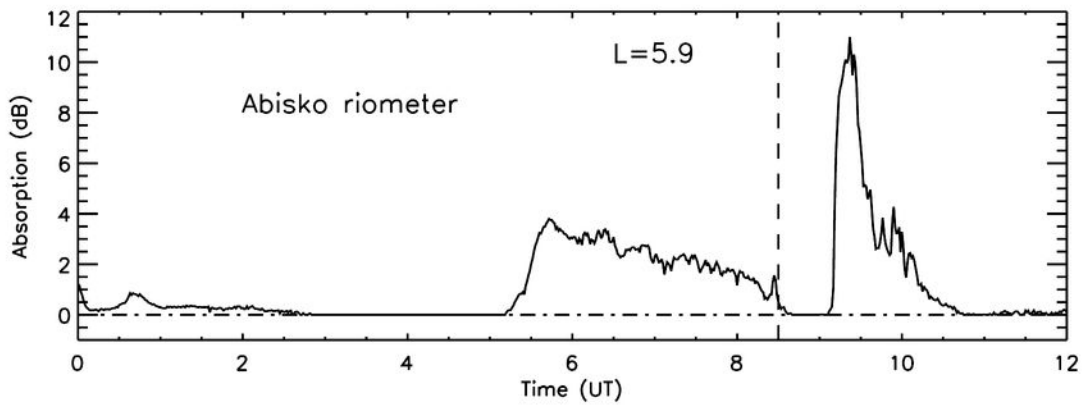
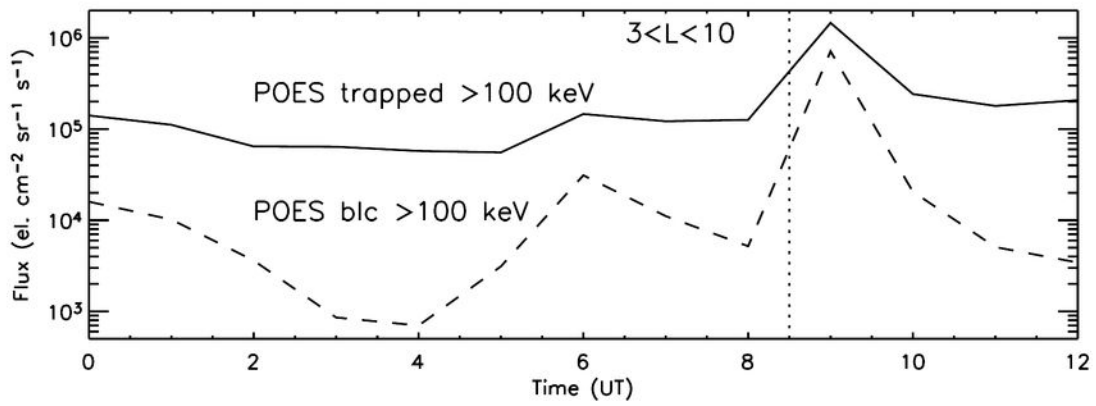
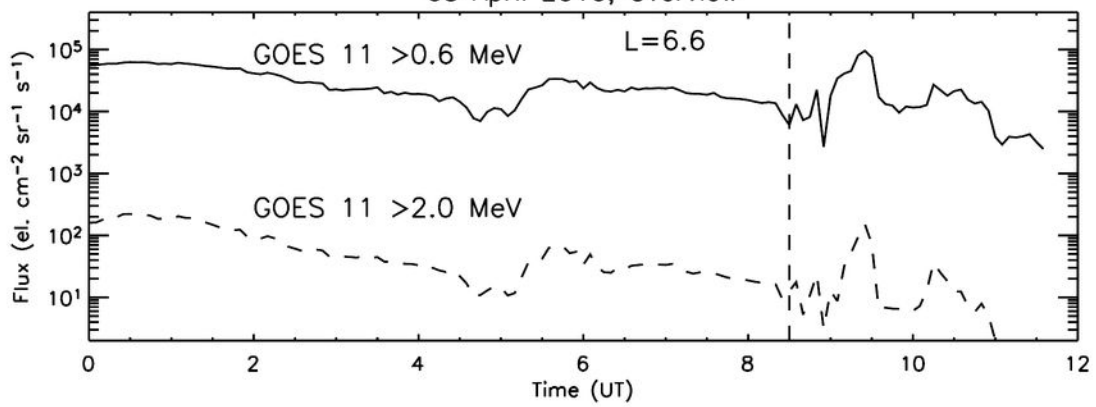
Station locations at 06 UT



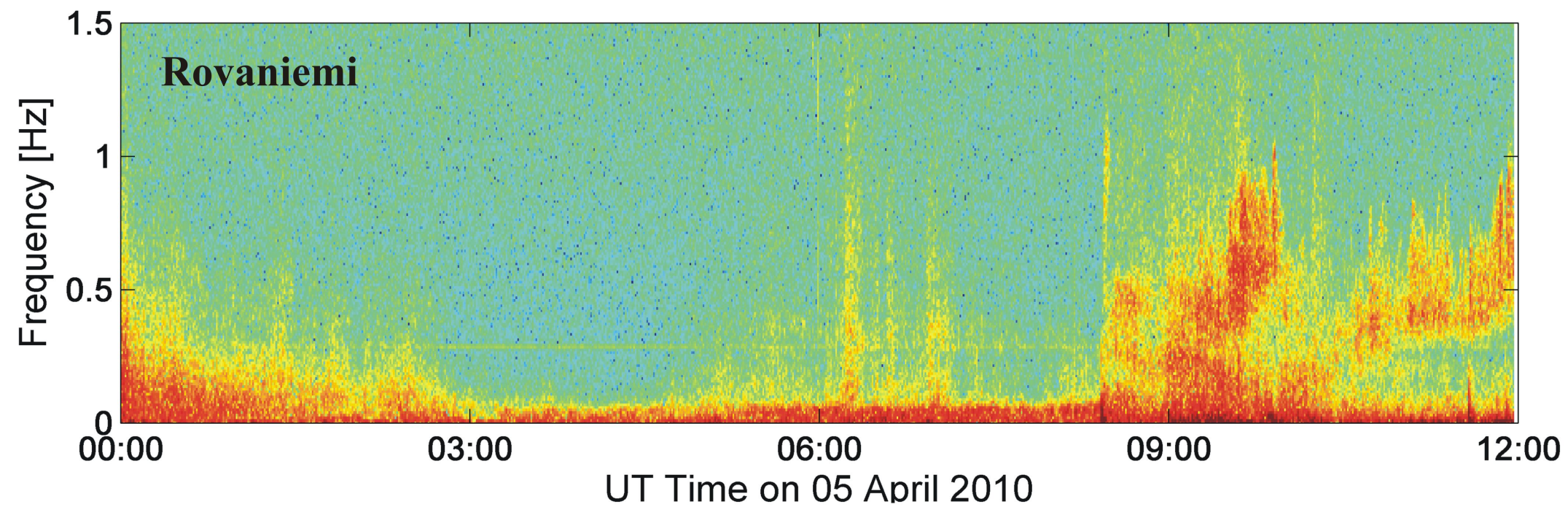
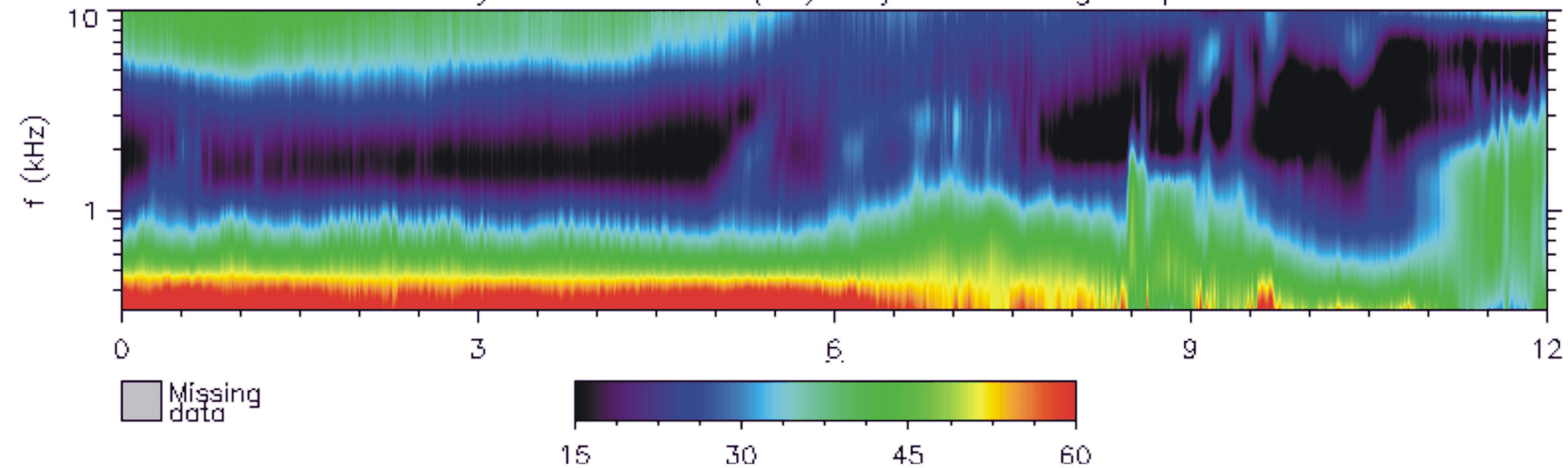
Station locations at 09 UT

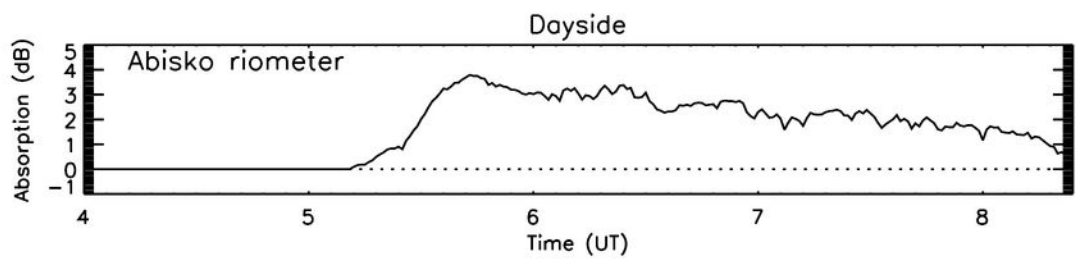
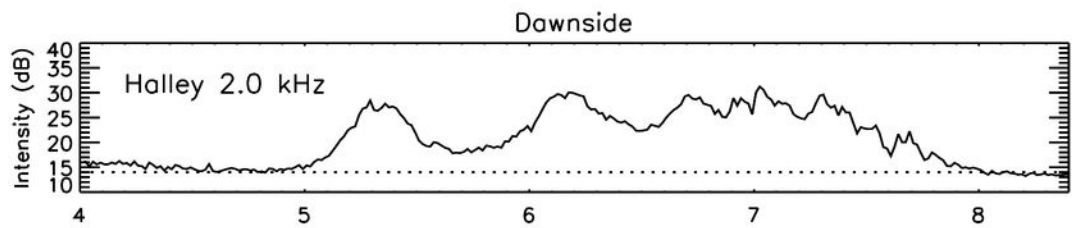
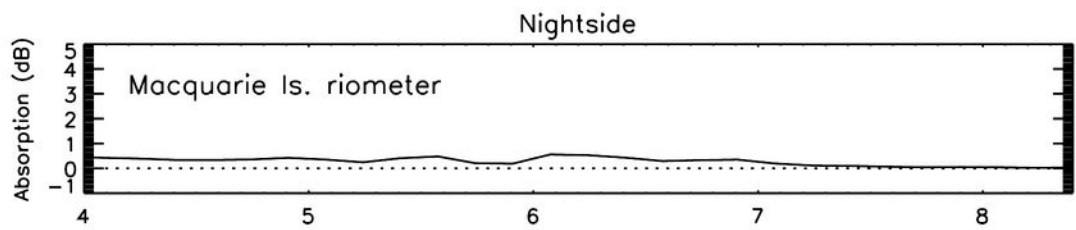
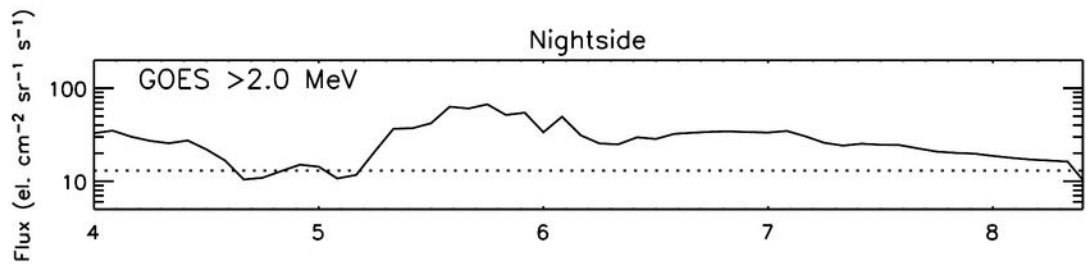
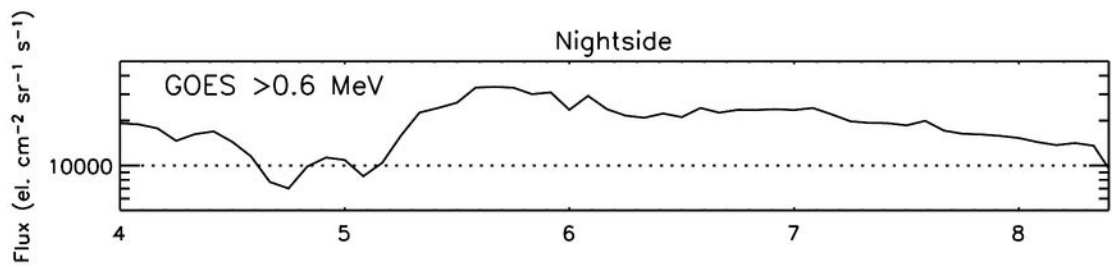


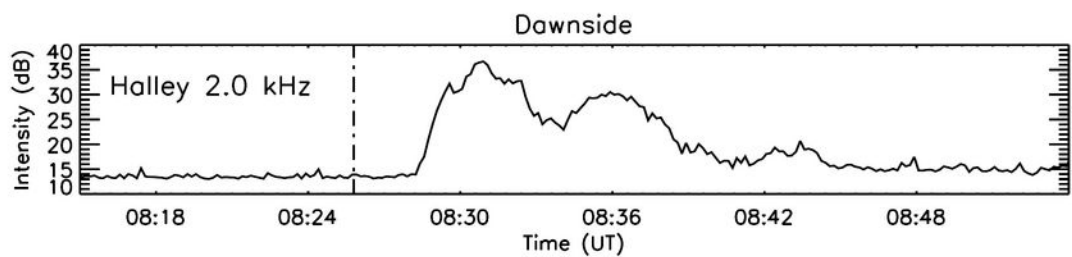
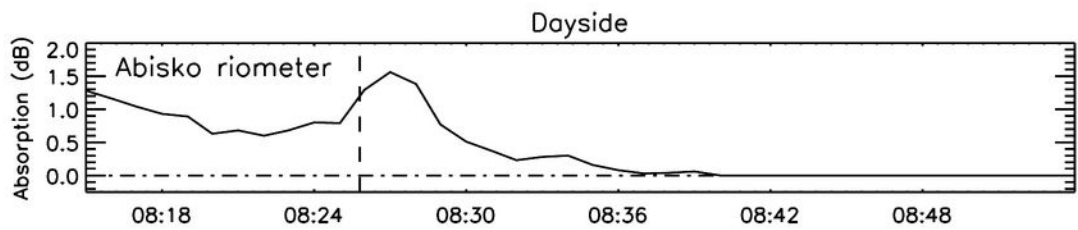
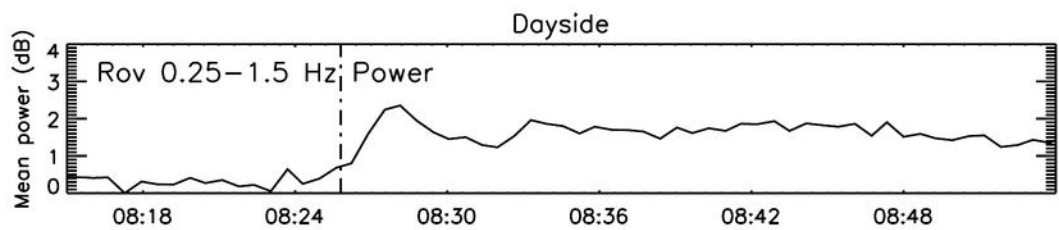
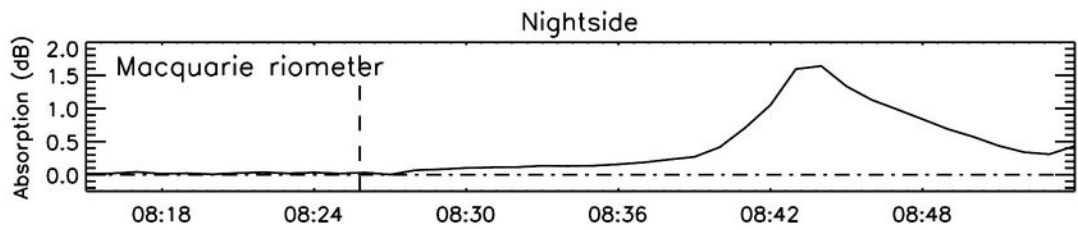
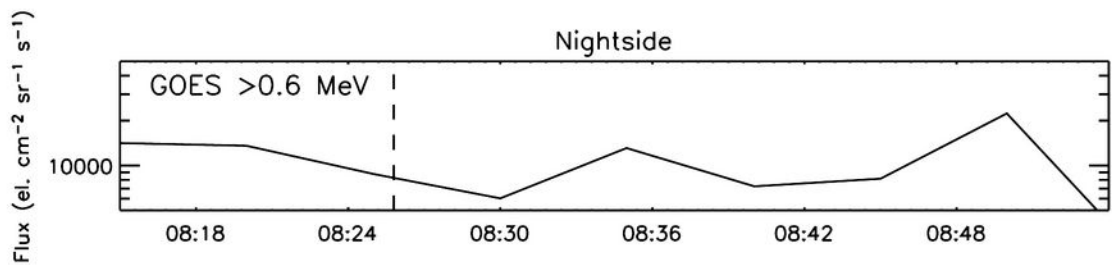
05 April 2010, Overview

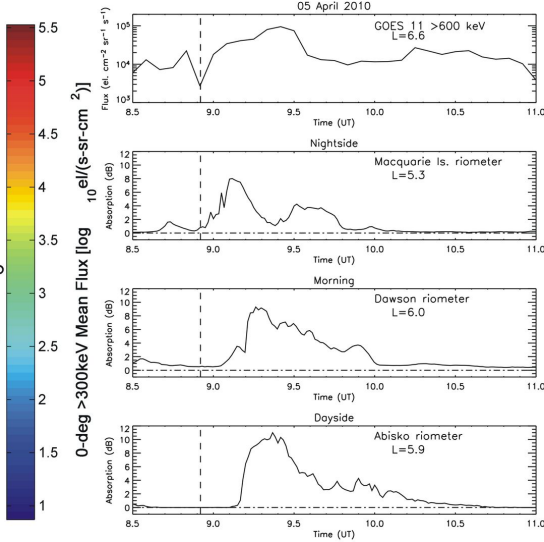
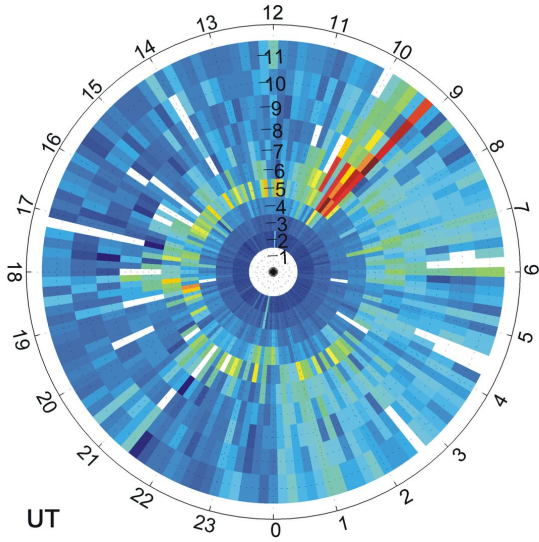


Halley 2010-04-05 (Day 95) Mean log amplitude

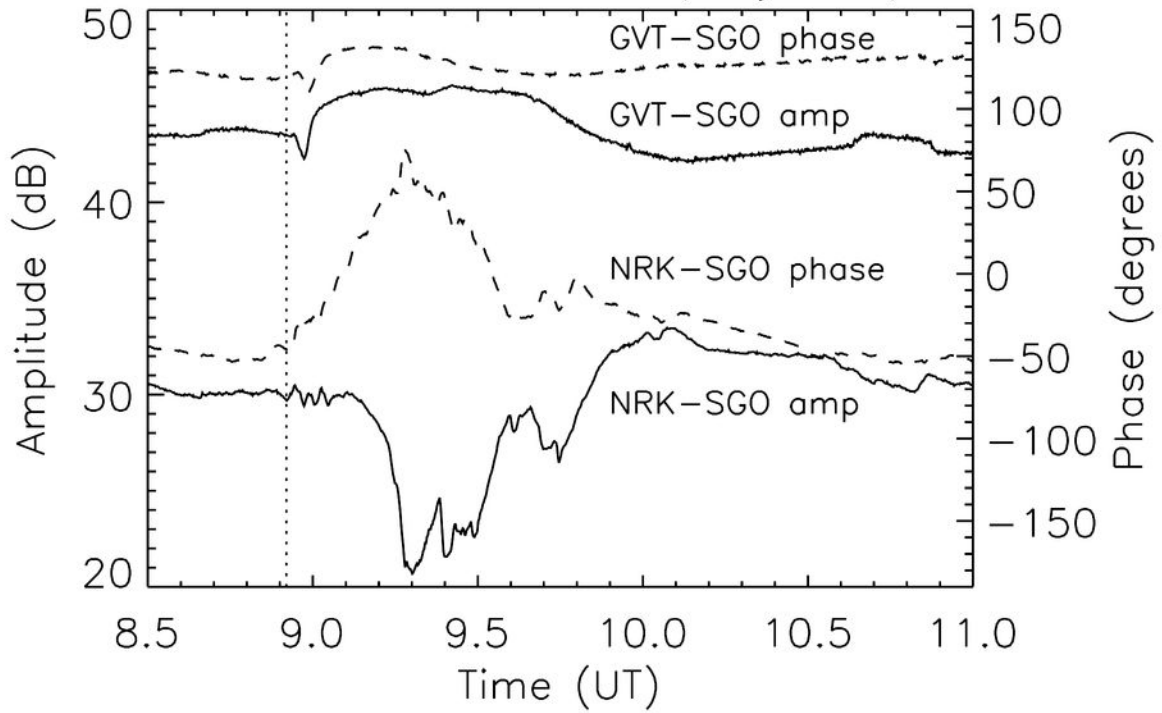








### AARDDVARK data (Dayside)



### AARDDVARK data (Nightside)

